Large-Eddy Simulation of Evaporatively Driven Entrainment in Cloud-Topped Mixed Layers

TAKANOBU YAMAGUCHI AND DAVID A. RANDALL

Department of Atmospheric Science, Colorado State University, Fort Collins, Colorado

(Manuscript received 1 March 2007, in final form 19 July 2007)

ABSTRACT

Cloud-top entrainment instability (CTEI) is a hypothesized positive feedback between cloud-top entrainment and enhanced turbulence associated with buoyancy reversal. A sufficiently strong positive feedback is hypothesized to lead to the destruction of the cloud. Numerous studies have investigated the possible role of CTEI in cloud breakup, with ambiguous results.

In this study, CTEI has been extensively investigated using many large-eddy simulations. An idealized experimental design has been used so as not to have any source of turbulence kinetic energy production except for entrainment due to evaporative cooling. A new method has been used to estimate the entrainment rate and to identify the inversion base and top.

The results of the experiments do show the hypothesized positive feedback when the Randall–Deardorff CTEI criterion is met. When CTEI takes place in the numerical experiments, entrainment develops spontaneously through buoyancy reversal and, as a result, leads to cloud dissipation. Cloud dissipation within several hours is simulated in the cases with strong instability. A hypothesized dependence of the strength of the evaporatively driven turbulence on the cloud-top liquid water mixing ratio is confirmed. As expected, with a typical stratocumulus liquid water mixing ratio, the evaporatively driven turbulence is weak.

Additional simulations with longwave radiation, surface latent heat flux, or both suggest that sufficiently strong radiative cooling can prevent cloud destruction by CTEI. For this reason, CTEI usually does not result in cloud dissipation in realistic cases.

1. Introduction

Cloud-top entrainment instability (CTEI) is a hypothesized positive feedback involving entrainment driven by evaporative cooling. It was first proposed by Lilly (1968), who suggested that a cloud layer would evaporate as a result of runaway entrainment if the equivalent potential temperature decreased upward across the cloud top.

When the warm and dry air from above a cloud is entrained, it is mixed with the cool and wet air of the cloud. Under certain conditions, evaporative cooling can make the mixture become denser than the cloudy air, so that it is accelerated downward by the buoyancy force (Fig. 1). The production of negatively buoyant mixtures that are denser than either of the "input" parcels is called buoyancy reversal (Siems et al. 1990, hereafter SB) and was mentioned by Squires (1958) in the context of penetrative downdrafts in cumuli.

Cloud-top entrainment normally consumes turbulence kinetic energy (TKE); this means that entrainment is associated with a sink term in the vertically integrated TKE budget equation. It is hypothesized, however, that in the presence of CTEI, the entrainment can lead to the generation of TKE through an upward buoyancy flux that is created as evaporatively cooled, negatively buoyant parcels accelerate downward away from the inversion.

Logically, the argument for the existence of CTEI can be decomposed into six hypothesized steps as in the left-hand column of Table 1. This chain of reasoning starts from the evaporative cooling of entrained air, then moves to buoyancy reversal, TKE production, and entrainment enhancement. The right-hand column of Table 1 lists issues regarding each step; these are discussed below.

Randall (1976, 1980) and Deardorff (1980) refined

Corresponding author address: Takanobu Yamaguchi, Colorado State University, Department of Atmospheric Science, 200 West Lake Street, Fort Collins, CO 80523-1371.
E-mail: tak@atmos.colostate.edu

DOI: 10.1175/2007JAS2438.1

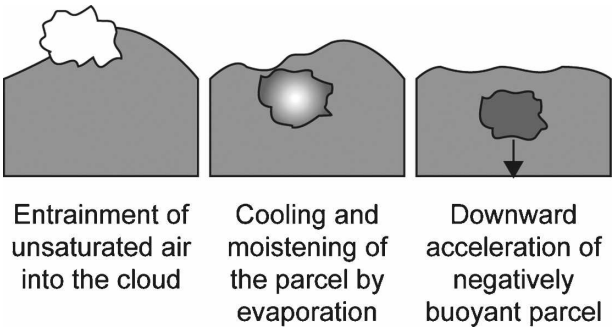

FIG. 1. A schematic illustration of CTEI, after Randall (1980).

Lilly's instability criterion by including the effects of water vapor and liquid water on the buoyancy of an entrained parcel. The Randall–Deardorff (hereafter RD) criterion is given by

$$\Delta_{\mathrm{RD}} \equiv \Delta s_v - (\Delta s_v)_{\mathrm{crit}} < 0, \tag{1}$$

where $\Delta() \equiv ()_{B+} - ()_B$ is the jump across the mixed layer top, the subscripts $B+$ and B denote levels just above and just below the cloud top, respectively, and s_v is the virtual dry static energy, which is often used as a measure of buoyancy:

$$s_v \equiv c_p T(1 + \delta r - l) + gz. \tag{2}$$

Here c_p is the specific heat of dry air at constant pressure; T is temperature; $\delta \equiv (R_v - R_a)/R_a \approx 0.608$, where R_a and R_v are the gas constants of dry air and water vapor, respectively; r is the total water mixing ratio; l is the liquid water mixing ratio; g is the gravitational acceleration; and z is height. Importantly, the derivation of (1) entails the assumption that the air at level B is uniformly saturated, despite the presence of parcels that consist in part of very dry air from level $B+$.

The parameter $(\Delta s_v)_{\mathrm{crit}}$, which appears in (1), is a measure of the dryness of the air above the PBL top and is always positive or zero. As shown by Randall (1976, 1980) it is given by

$$(\Delta s_v)_{\mathrm{crit}} = \left[\frac{1 - (1 + \delta)\epsilon}{1 + \gamma}\right] L(q^*_{B+} - q_{B+}), \tag{3}$$

where q^* is the saturation mixing ratio, q is the water vapor mixing ratio, L is the latent heat, and

$$\begin{cases} \epsilon \equiv \dfrac{c_p T}{L} \\ \gamma \equiv \dfrac{L}{c_p}\left(\dfrac{\partial q^*}{\partial T}\right)_p, \end{cases} \tag{4}$$

where p is the pressure.

TABLE 1. An analysis of the CTEI hypothesis.

	What is hypothesized to happen	Issues
Step 1	Newly entrained air, which is initially warm and dry, is cooled by the evaporation of cloud water.	Although there is little question that such evaporative cooling does occur, its magnitude is limited by the small cloud water mixing ratios that are typical of marine stratocumulus clouds (Albrecht et al. 1985).
Step 2	The evaporative cooling makes it easier for the entrained air to sink into the PBL, and so it favors faster entrainment, all other things being equal.	This is probably true, but the effect is not very well understood and has not been adequately quantified.
Step 3	When the CTEI criterion is satisfied, the evaporative cooling of recently entrained air leads to the "spontaneous" production of negatively buoyant parcels.	This is questionable because of the modest evaporative cooling associated with the low liquid water mixing ratios, as mentioned above.
Step 4	Presuming that the entrained air does actually become negatively buoyant, it then sinks under the action of the buoyancy force, leading to a positive (upward) flux of virtual temperature, i.e., $\overline{w'\theta'_v} > 0$.	The analyses used to predict (e.g., Randall (1980)) this assume that the cloud layer is uniform, and this is not likely to be the case if there is rapid entrainment of dry, warm air.
Step 5	The hypothesized positive buoyancy flux promotes turbulence in the PBL.	Moeng (2000) showed no production of strong TKE when CTEI occurred in her simulations.
Step 6	This turbulence, in turn, promotes entrainment, thus closing a positive feedback loop with step 1 above.	The assumption of enhanced entrainment is certainly questionable. Even if it is true that cold blobs of air are vigorously sinking away from the upper portion of the PBL, it is not clear that this will significantly enhance the rate of entrainment, which is thought to be associated with updrafts that overshoot into the inversion. In other words, it is possible that turbulence associated with evaporative cooling does not entrain very efficiently.

Previous studies provide evidence both for and against the existence and importance of CTEI. Some numerical studies, performed in the early 1980s, supported the CTEI hypothesis; for example, Deardorff (1980) simulated cloud breakup, possibly due to CTEI, in a low-resolution large-eddy simulation (LES). CTEI may also play a role in the cloud breakup simulated by Moeng and Arakawa (1980), who used a second-order closure model with a large domain but coarse resolution. However, most studies performed in the 1980s did not support the CTEI hypothesis, and many provided evidence against it (e.g., Mahrt and Paumier 1982; Hanson 1984a,b; Albrecht et al. 1985, hereafter APS; Nicholls and Turton 1986; Tag and Payne 1987; Kuo and Schubert 1988, hereafter KS). For instance, KS used many stratocumulus observations to show that solid cloud decks often persist even though the RD criterion is satisfied. KS expressed the RD criterion as

$$\Delta\theta_e < \kappa\left(\frac{L}{c_p}\right)\Delta r, \tag{5}$$

where θ_e is equivalent potential temperature. They stated that

$$\kappa > 0.23 \quad \text{for} \quad \Delta_{\mathrm{RD}} < 0. \tag{6}$$

As discussed in appendix A, the value of κ required for instability actually depends on the temperature near the cloud top.

APS pointed out that with typical stratocumulus cloud water amounts buoyancy reversal can produce only slight cooling of mixtures, relative to the cooler of the two input parcels. Further discussion of this point can be found in the work of Nicholls and Turton (1986), KS, SB, and Shao et al. (1997). APS introduced a mixing fraction χ and considered parcels consisting of a fraction χ of air from level $B+$ and the remaining fraction $1 - \chi$ from level B. For such a mixed parcel, a moist conservative variable (e.g., moist static energy, $h \equiv c_p\, T + Lq + gz$) of the mixture h_{mix} should satisfy

$$h_{\mathrm{mix}} = h_{B+}\chi + h_B(1 - \chi), \tag{7}$$

where $0 \le \chi \le 1$. APS pointed out that the buoyancy, $s_v - (s_v)_B$, of a mixed parcel cannot be more negative than the buoyancy at the saturation mixing fraction, χ^*, which is defined to be the value of χ at exact saturation (Fig. 2). Shao et al. (1997) show that

$$\chi^* = \frac{[1 - (1 + \delta)\epsilon]Ll_B}{[1 - (1 + \delta)\epsilon]Ll_B + (\Delta s_v)_{\mathrm{crit}}}. \tag{8}$$

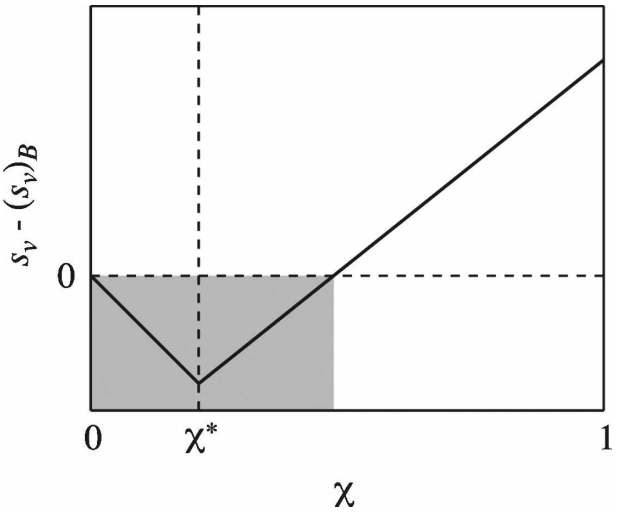

FIG. 2. Relationship between mixing fraction and buoyancy. An air parcel is neutrally buoyant for $\chi = 0$ or $s_v = (s_v)_B$ and positively buoyant for $\chi = 1$ or $s_v = (s_v)_{B+}$. The parcel is negatively buoyant in the shaded region. If $\chi < \chi^*$, CTEI can take place according to the RD criterion, which assumes uniformly cloudy air.

Saturation occurs for $0 \le \chi \le \chi^*$. Inspection of (8) shows that $\chi^* = 0$ for $l_B = 0$, and that χ^* approaches 1 for large l_B. Shao et al. (1997) also show that

$$(s_v)_{\mathrm{at}\ \chi^*} - (s_v)_B = \chi^*\Delta_{\mathrm{RD}}\ (< 0), \tag{9}$$

where $(s_v)_{\mathrm{at}\ \chi^*} - (s_v)_B$ is the strongest possible negative buoyancy. It follows from (8) and (9) that stronger negative buoyancy can be produced with a larger cloud-top liquid water mixing ratio, l_B. Therefore, the strength of the evaporatively driven turbulence may depend on l_B. However, χ^* is small (<0.1) for typical stratocumulus clouds, because of small cloud-top liquid water mixing ratios ($\lesssim 0.3$ g kg^{-1}). APS therefore concluded that CTEI is unlikely to occur.

Randall (1984) pointed out the possibility of cloud deepening through entrainment (CDE), in which the cloud top rises faster than the cloud base. He showed that CTEI and CDE can exist simultaneously and suggested that CTEI might be masked, in some cases, by CDE. Tag and Payne (1987) found that CDE could not explain their simulation of a long-lasting uniform cloud with $\Delta_{\mathrm{RD}} < 0$. They concluded that the relationship between the RD criterion and cloud breakup is very weak.

During the 1990s, while observational studies continued to provide evidence against the CTEI hypothesis (e.g., Weaver and Pearson 1990; Albrecht 1991; Khalsa 1993; Wang and Albrecht 1994), several alternative stability criteria were proposed (SB; MacVean and Mason 1990, hereafter MM; Duynkerke 1993). Various pro-

TABLE 2. List of proposed CTEI criteria.

Criteria	Formula	References	Comment
RD	$\Delta_{RD} < 0$	Randall (1976, 1980); Deardorff (1980)	This criterion is derived with the assumption that mixed air is saturated.
KS	$\kappa > 0.23$	Kuo and Schubert (1988)	This is equivalent to the RD criterion.
SB	$D > 1.3$	Siems et al. (1990); Shy and Breidenthal 1990)	SB considered the ratio of the strongest possible negative buoyancy to the inversion strength. $D = 0$ for $\Delta_{RD} = 0$.
MM	$\kappa > 0.7$	MacVean and Mason (1990)	This criterion is derived through an analysis of a potential-to-kinetic energy conversion between clear and cloudy layers.
DK	$\Delta_a < 0$	Duynkerke (1993)	This criterion is derived by consideration of the total buoyancy of a parcel per unit mass of entrained air. It reduces to the RD criterion with large liquid water content.
LL	$\frac{-L\Delta r}{c_p\Delta\theta_l} > \kappa_L$	Lilly (2002)	This criterion is derived from the dependency of the buoyancy flux on the entrainment rate in Lilly's (2002) new entrainment rate parameterization. The value of κ_L decreases with lower cloud base height and larger cloud-top wetness. In a limit, it reduces to the RD criterion.

posed CTEI criteria are listed in Table 2. In this table, we include not only criteria proposed in the 1990s and earlier but also a criterion recently proposed by Lilly (2002). Further discussion is given in appendix A.

Eddy-resolving numerical studies (e.g., SB; Siems and Bretherton 1992; Krueger 1993; MacVean 1993; Moeng et al. 1995) open the door to a possible new view of CTEI: that cloud breakup is not always the end result. SB, Siems and Bretherton (1992), and Krueger (1993) concluded that cloud destruction by CTEI is unlikely if the SB criterion is correct, and that the CTEI hypothesis is probably not relevant to real stratocumulus clouds. MacVean (1993) concluded that CTEI might be an important mechanism for rapid cloud breakup only in case of large κ as in the MM criterion (see Table 2). Moeng et al. (1995) suggested that cloud breakup is governed by a competition between the hypothesized positive entrainment–evaporation feedback (i.e., CTEI) and a negative entrainment–radiation feedback. The entrainment–radiation feedback is negative because the amount of time that the entrained air is exposed to radiative cooling is reduced when the entrainment rate is rapid. If the negative feedback associated with radiative cooling dominates the positive feedback of CTEI, a cloud can persist even when the RD criterion is satisfied.

The processes that are hypothesized to be at work in CTEI (Table 1) have also been studied with LES. For example, Lewellen and Lewellen (1998) found that evaporative cooling promotes turbulence kinetic energy production when the RD criterion is satisfied. Lock and MacVean (1999) obtained an enhancement of entrainment due to buoyancy reversal.

To isolate the effects of buoyancy reversal on the fractional cloudiness of the PBL, M. K. MacVean and C. S. Bretherton (1999, unpublished manuscript, hereafter MB) performed five high-resolution two-dimensional LES with an idealized model configuration, which allowed only evaporatively driven entrainment. They found that a cloud eventually breaks up and is completely dissipated by buoyancy reversal when $\Delta_{RD} < 0$, if there are no processes other than the turbulence and entrainment associated with evaporative cooling. The SB and MM criteria did not appear to be relevant, since cloud breakup took place when the cloud was stable by both the SB and MM criteria, but unstable by the RD criterion.

Moeng (2000) also found that the liquid water path (LWP) and cloud fraction decreased if and only if the RD criterion was satisfied. In her LESs, however, neither rapid entrainment nor strong TKE production were produced. An interpretation of her results is that the positive CTEI feedback is weak.

With observational data acquired in the Second Dynamics and Chemistry of the Marine Stratocumulus field study (DYCOMS-II; Stevens et al. 2003), Gerber et al. (2005) showed that the cloud thickness increased during a time when CTEI would be expected according to the RD criterion. The authors argued that the radiative cooling at the cloud top maintained convection, which transported water vapor from the surface into the cloud fast enough to compensate for the evaporation of liquid water associated with the entrainment of dry air. This could explain the results of the LES intercomparison study based on DYCOMS-II (Stevens et al. 2005), under the auspices of the Global Energy and Water Cycle Experiment (GEWEX) Cloud System Study (GCSS). In the DYCOMS-II study, many models simulated a cloud fraction close to one even when CTEI would be expected according to the RD criterion. The effects of such cloud building processes are discussed later in this paper.

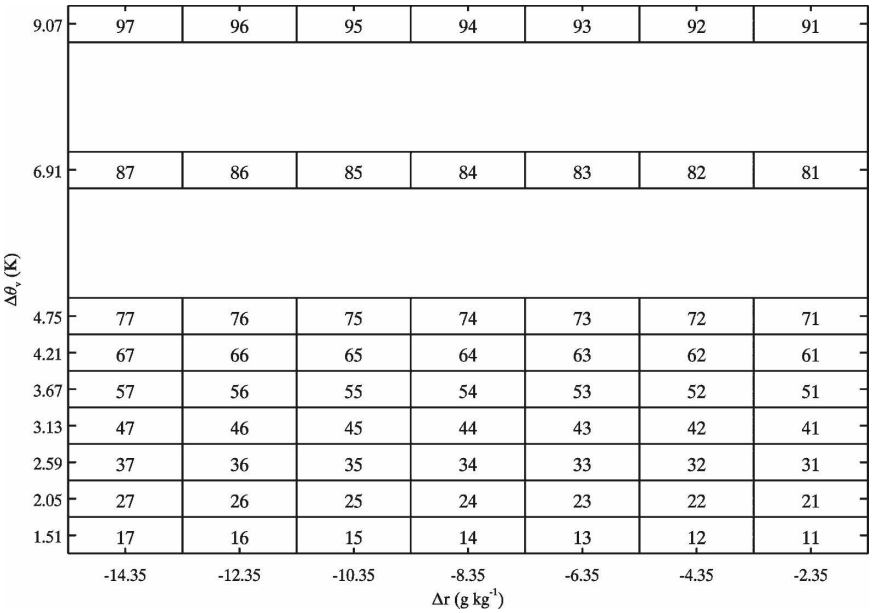

FIG. 3. Case indices of BR-0.5 depending on the jump values of moisture and buoyancy in the $\Delta\theta_v$-Δr plane. For example, jump values of case 65 are $\Delta\theta_v = 4.21$ K and $\Delta r = -10.35$ g kg^{-1}.

The results of the CTEI studies listed above have not been systematically linked with each other and explained as a whole. Rather, they have been treated as individual results in a "seesaw game." The APS theory allows only weak buoyancy reversal for real marine stratocumulus. The RD criterion is based on the assumption of uniformly saturated air. No strong generation of TKE and rapid entrainment is found in LES (Moeng 2000). Moeng's negative radiation feedback (Moeng et al. 1995; Gerber et al. 2005) has not been incorporated into an instability criterion.

Our approach is similar to that of MB; we have performed numerical experiments using three-dimensional LESs with entrainment due to buoyancy reversal as the only active process. Such idealized experiments, which we call buoyancy reversal (BR) experiments, can be used to test whether or not CTEI exists and to test proposed criteria for its onset, but they do not show what CTEI will do in realistic situations. For this reason, we also include one case based on real data, that is, DYCOMS-II (Stevens et al. 2005).

The next section presents a description of the design of the idealized experiments. The discussion covers a summary of the LES model used, tests of grid spacing sensitivity based on DYCOMS-II simulations, a method for diagnosing the entrainment rate, and a description of our DYCOMS-II simulation. In section 3, the results of the BR experiments are shown and analyzed. Conclusions are presented in section 4. We also provide a list of abbreviations in appendix B.

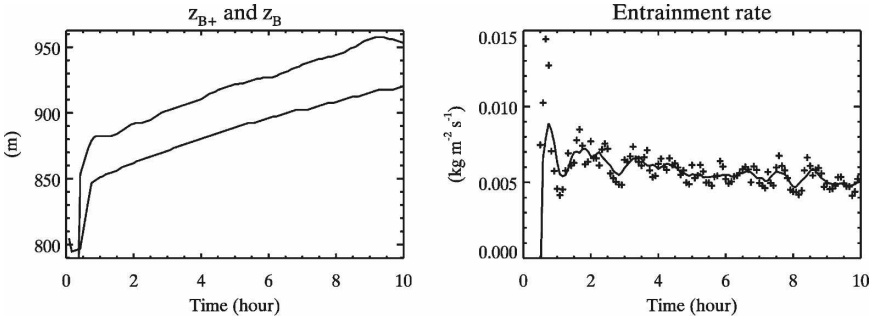

FIG. 4. Time series of diagnosed z_B and z_{B+} and entrainment rate for the DYCOMS-II simulation. For the solid line of the entrainment rate, a 30-min running mean was used for smoothing.

2. Design of the buoyancy reversal experiments

a. LES model

We performed all LESs with the System for Atmospheric Modeling (SAM), developed at the University of Oklahoma and at Colorado State University (Khairoutdinov and Randall 2003). The model was first used to develop and test a bulk microphysics scheme (e.g., Khairoutdinov and Kogan 1999, 2000); the bulk scheme is used in this study. It has also been employed in the GCSS studies of the First International Satellite Cloud Climatology Project Regional Experiment (FIRE; Moeng et al. 1996), an idealized smoke cloud case (Bretherton et al. 1999), the Barbados Oceanographic and Meteorological Experiment (BOMEX; Siebesma et al. 2003), and DYCOMS-II (Stevens et al. 2005).

The dynamical core of SAM is based on the anelastic equations. The thermodynamic prognostic variables are liquid–ice water static energy, total nonprecipitating water (vapor + cloud water + cloud ice), and total precipitating water (rain + snow + graupel). SAM diagnoses the cloud condensate (cloud water + cloud ice) and determines the partitioning of the cloud condensate and the total precipitating water into the hydrometeor mixing ratios based on temperature. Third-order Adams–Bashforth time differencing (Durran 1991) is used. The Arakawa C grid is employed, and the momentum equation is solved using second-order finite differences in flux form, conserving kinetic energy under advection. We used the default subgrid-scale (SGS) model, which is a 1.5-order closure based on a prognostic SGS TKE. The lateral boundaries are periodic, and a rigid boundary is assumed at the domain top. Damping of gravity waves can be selected and was used in all of our runs. The surface fluxes are computed based on Monin–Obukhov similarity (Monin and Obukhov 1954). The radiation scheme can be selected from one of two options: the National Center for Atmospheric Research Community Climate Model version 3 (CCM3; Kiehl et al. 1998) or a simple radiative transfer code as specified, for example, in some GCSS studies. Finally, the model can be run on parallel computers, through use of the Message Passing Interface.

b. Setting, cases, series, and soundings

In the BR experiments, the only (potential) TKE source is evaporatively driven entrainment, that is, buoyancy reversal. We do not include other processes that could influence the evolution of the cloud, such as large-scale subsidence, surface fluxes, shortwave and longwave radiation, and precipitation. The thermodynamic initial conditions in the first 30 m above the

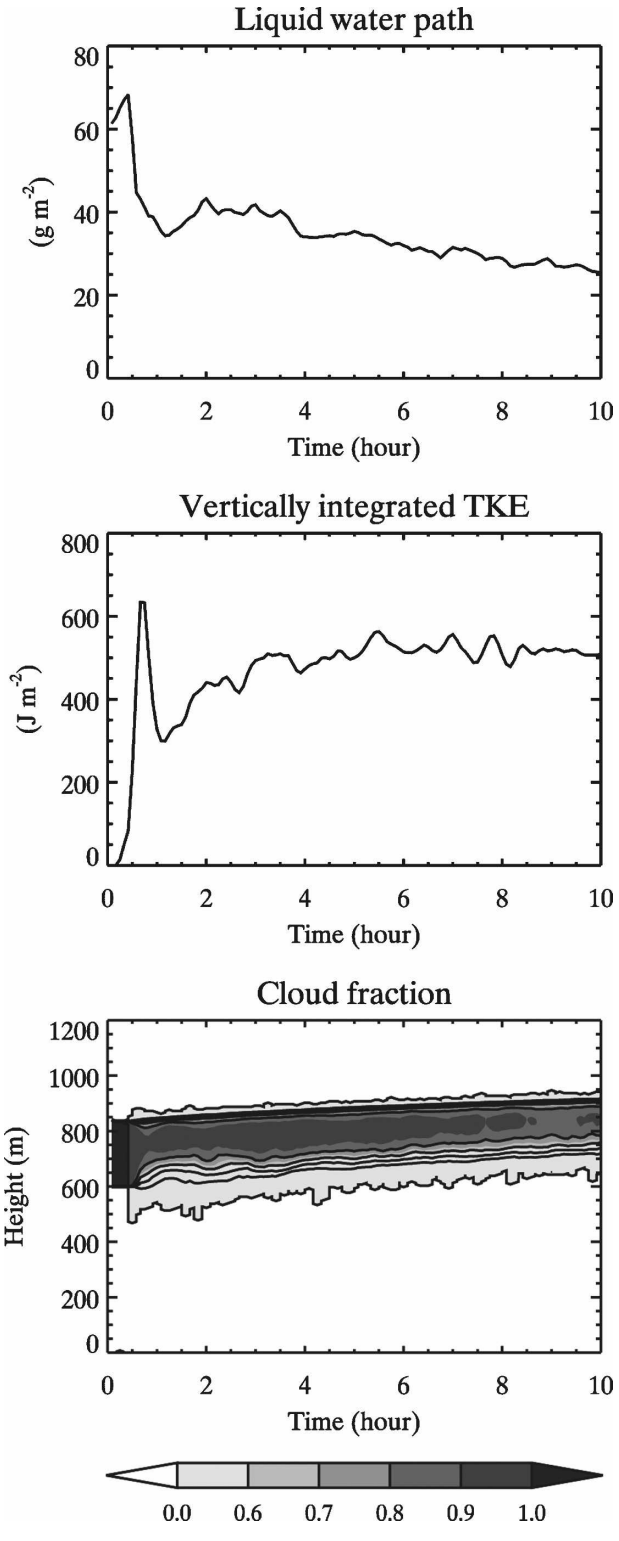

FIG. 5. Time series of liquid water path, vertically integrated TKE, and cloud fraction. For the cloud fraction, contour lines are drawn every 0.2, and the cloud fraction between 0 and 0.6 is colored with the lightest gray. Compare with Fig. 2 of Stevens et al. (2005).

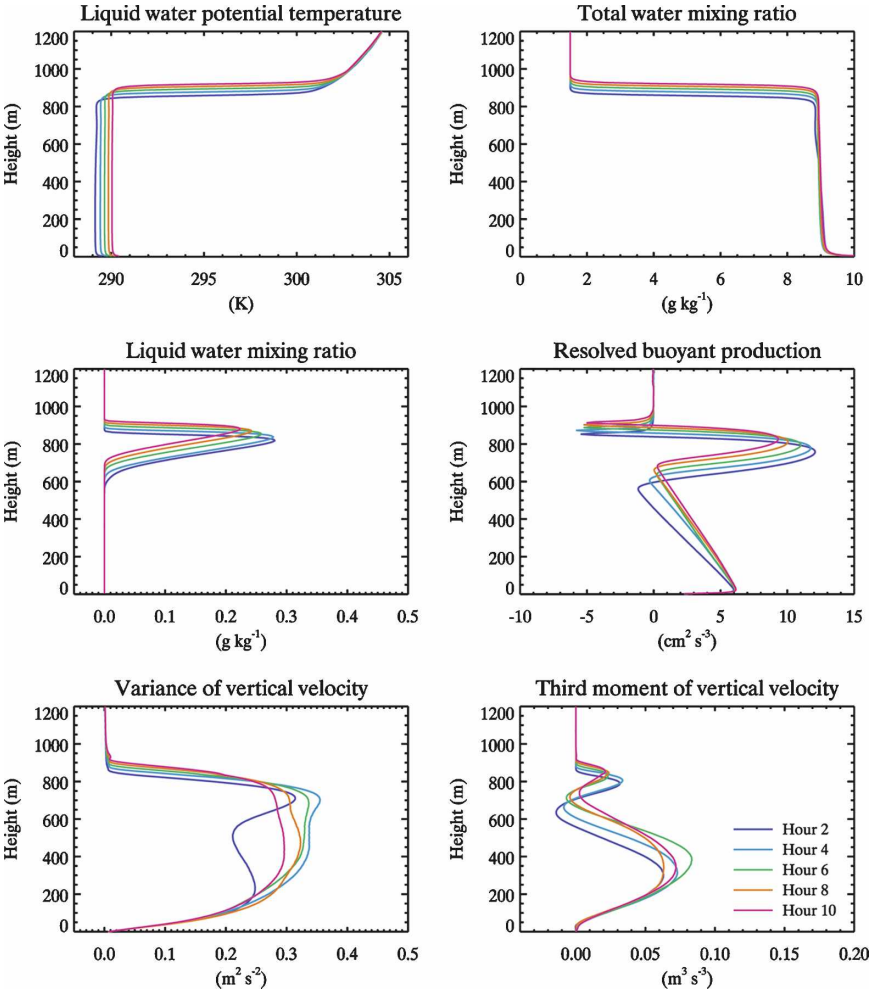

FIG. 6. One-hour-averaged vertical profiles of liquid water potential temperature, total mixing ratio, liquid water mixing ratio, resolved buoyant production of TKE, variance of vertical velocity, and third moment of vertical velocity. Profiles are drawn every 2 h. Refer to Figs. 4 and 5 of Stevens et al. (2005).

lower boundary are perturbed slightly so as to (potentially) trigger entrainment associated with evaporative cooling. After the initialization, the model runs freely for 10 simulated hours.

The BR experiments include three series, which we call BR-0.5, BR-1, and BR-2. BR-0.5 is the "baseline" series and consists of 63 cases. BR-1 and BR-2, with 49 cases per series, are designed to test the effects of the increased cloud-top liquid water amount, l_B, as discussed later.

Each series has a single sounding for the mixed layer and range of soundings for the free troposphere. The series differ in the amount of moisture within the mixed layer. For the BR-0.5 series, l_B is set to 0.5 g kg^{-1}. For the BR-1 series, we set l_B to 1 g kg^{-1}. For the BR-2 series, we set l_B to 2 g kg^{-1}. The mixed layer soundings used with BR-1 and BR-2 were generated so as to produce these increased liquid water mixing ratios without changing Δ_{RD}.

For the free troposphere, we generated a range of soundings, which were the same for BR-0.5, BR-1, and BR-2. Each sounding was created based on a combination of different "jumps" of the virtual potential temperature, θ_v, and total mixing ratio. Figure 3 shows the jumps used for each case of BR-0.5 to produce free tropospheric soundings. It should be noted that these soundings are idealized, and some of them might not be expected to occur with marine stratocumulus clouds, for example, those with very weak inversion strengths. Cases 81 through 97 were simulated only for BR-0.5 to see the effects of the stronger inversion. For BR-1 and BR-2, all remaining cases were simulated. The details

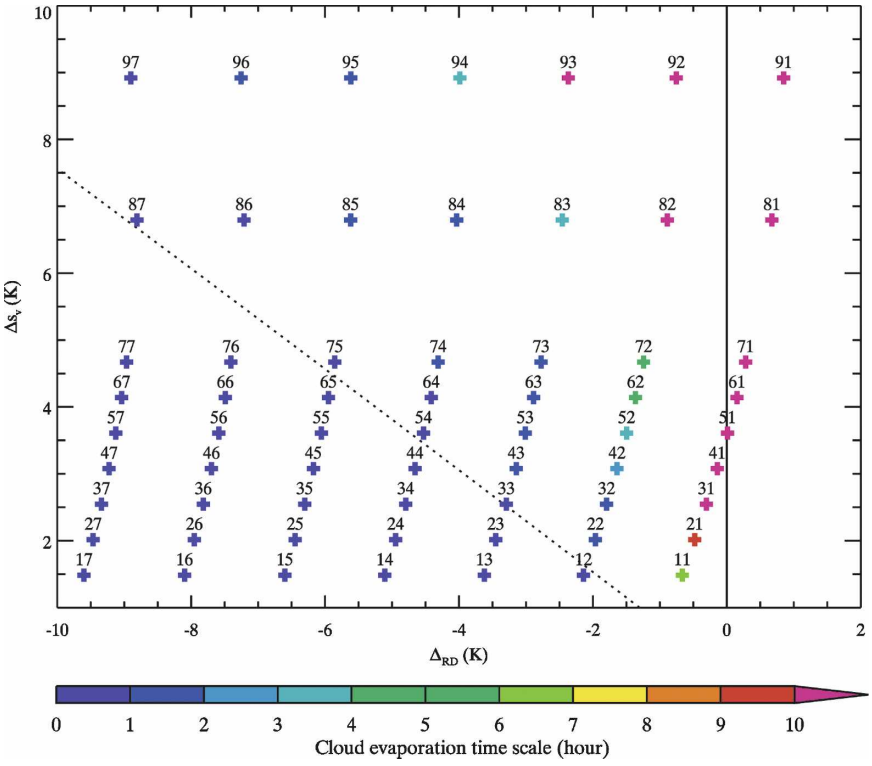

FIG. 7. CTEI diagram of BR-0.5. The solid line is a theoretical boundary corresponding to the RD criterion, such that instability occurs to the left of the line. The dotted line is a theoretical boundary for the SB criterion. Color indicates the cloud evaporation time scale in hours, as defined in the text.

of our method to generate the soundings are explained in appendix C.

c. Selecting the grid spacing

We selected a horizontal grid spacing of 50 m and a vertical grid spacing of 5 m for the BR experiments. Three grid spacings, $(\Delta x, \Delta z) = (35, 5)$, (50, 5), and (50, 10) m, where Δx (Δz) is horizontal (vertical) grid spacing, were tested for the GCSS DYCOMS-II simulation (Stevens et al. 2005). Comparison of the results suggested that the choice $(\Delta x, \Delta z) = (50, 5)$ gives results very similar to those obtained with $(\Delta x, \Delta z) = (35, 5)$ in 10-h simulations. The general results of the run with $(\Delta x, \Delta z) = (35, 5)$ are summarized in section 2e. Further details of the comparison are presented in appendix D. We selected a width of 3.2 km for the horizontal domain, which is about the same size as used in the DYCOMS-II simulation. We selected a 1.25-km domain depth; the BR experiments have an initial cloud top at 500 m, which is about 300 m lower than DYCOMS-II.

According to a scaling analysis suggested by Bretherton et al. (1999), the 5-m vertical grid spacing is not quite sufficient to resolve entrainment for all of the cases. However, this grid spacing is consistent with that used by Stevens et al. (2005).

d. Diagnosis of the entrainment rate

In the course of our analysis, we need to diagnose the entrainment rate from the LES results. The diagnosis of the entrainment rate must involve the diagnosis of the heights of levels B and $B+$, which is not straightforward. The dry mixed layer's top is typically defined as the level of the most negative buoyancy flux, but there is no simple way to estimate the inversion height of a cloudy mixed layer. Recently, Moeng et al. (2005) proposed a method to determine the depth of a stratocumulus-topped mixed layer.

Although the development of a diagnostic method to determine the mixed layer top and inversion height is an immature subject and is not our primary focus, we developed our own method to find levels B and $B+$. Our method utilizes the inversion-layer budget equations of mixed layer theory, first derived by Lilly (1968), to formulate a quadratic function of the entrainment rate. We find the entrainment rate that is most compatible with the mixed layer theory. Figure 4 shows the

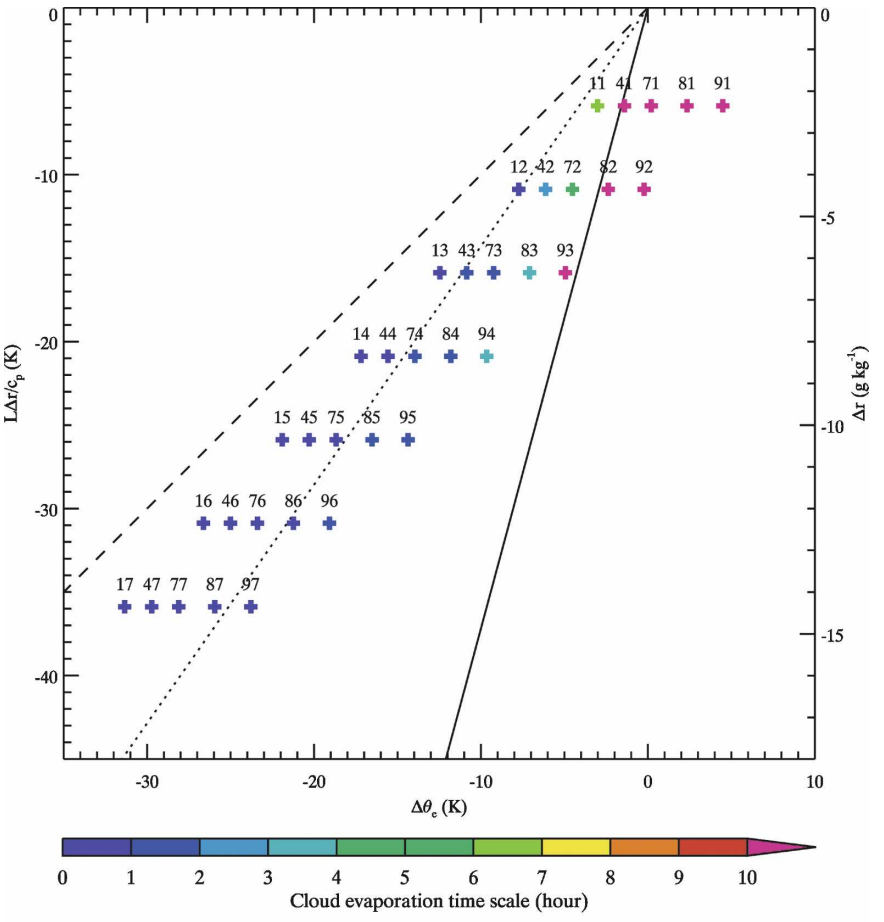

FIG. 8. CTEI diagram for BR-0.5, plotted for comparison with the KS criterion. The solid line is the stability boundary, where $\kappa = 0.27$. The dotted line is the stability boundary for the MM criterion ($\kappa = 0.7$), and the dashed line is $\kappa = 1$. Compare with Fig. 1 of Kuo and Schubert (1988).

results from the DYCOMS-II simulation obtained with the method explained here. Our method diagnosed an entrainment rate consistent with the results of Stevens et al. (2005). The details are explained in appendix E.

e. Summary of a GCSS DYCOMS-II run

Before leaving this section, we summarize the results of a DYCOMS-II simulation. SAM was configured as in Stevens et al. (2005) and run for 10 simulated hours. The domain size was 3.36 km horizontally and 1.6 km vertically. The horizontal grid spacing was 35 m and the vertical grid spacing was 5 m.

Figure 5 shows the time evolutions of LWP, vertically integrated TKE, and cloud fraction as presented in Fig. 2 of Stevens et al. (2005). For the first 4 h, these results agree well with those of the GCSS study. There is a tendency for continuously decreasing LWP and a slight increasing trend of TKE. The cloud fraction is more than 0.9 for most of the time. The cloud top and base are slowly rising throughout the simulation.

Figure 6 shows the corresponding 1-h averaged vertical profiles of various quantities, shown every 2 h. The profiles for hour 4 correspond to those in Figs. 4 and 5 of the GCSS study and agree with them. There is a slight deepening of the PBL after 10 h. During this deepening, the cloud becomes drier, as one can see from the decreasing liquid water mixing ratio. Resolved buoyant production of TKE, which is closely related to the buoyancy flux, is negative at the top of the subcloud layer for hours 2 and 4. This might be evidence for decoupling, which is traditionally defined as the existence of a sufficiently large negative buoyancy flux at the top of the subcloud layer. However, the magnitudes of the buoyancy integral ratio proposed by Turton and Nicholls (1987) and Bretherton and Wyant (1997), who

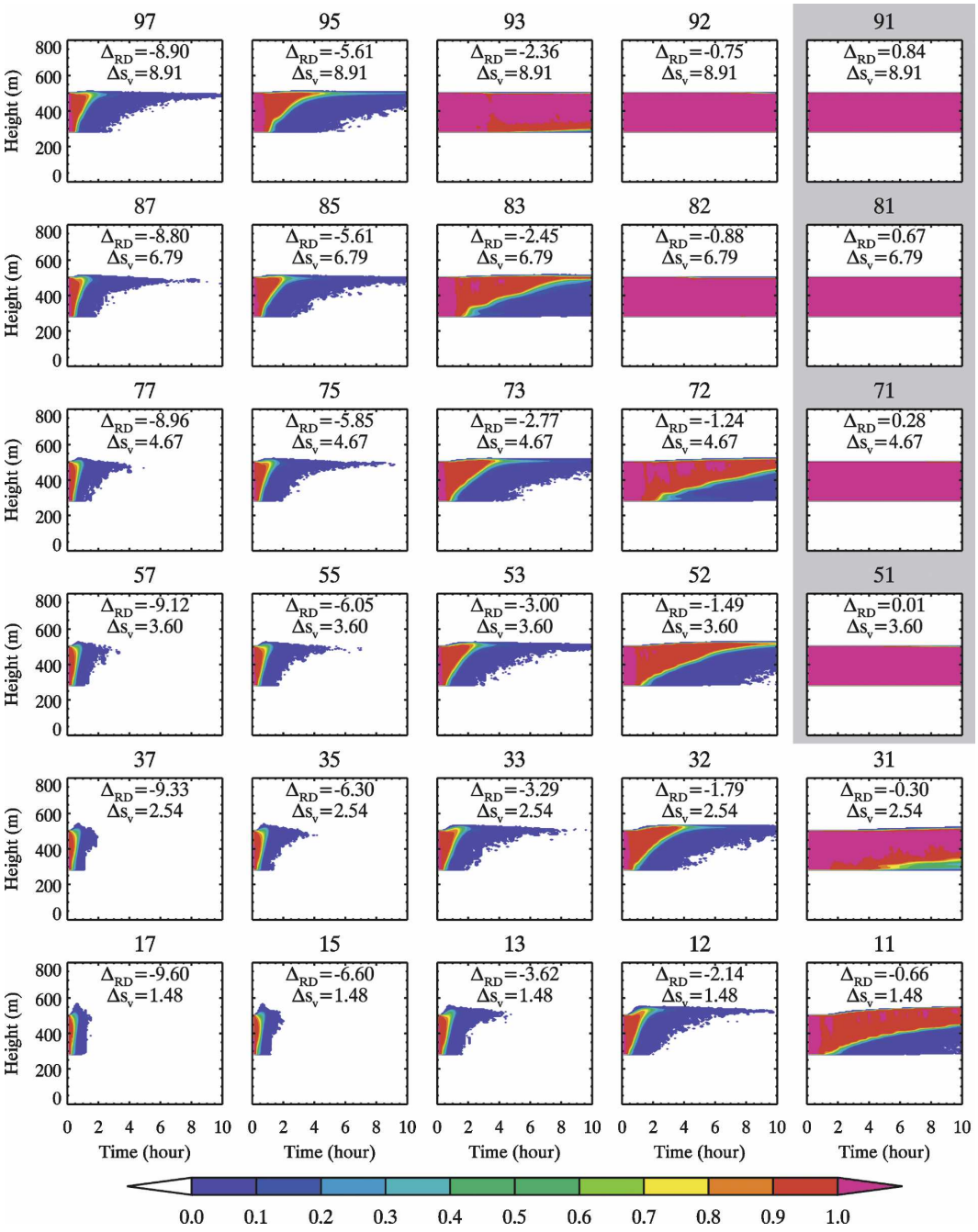

FIG. 9. Time evolution of cloud fraction with the initial Δs_v and Δ_{RD} of each case for a subset of the BR-0.5 cases. Spatial arrangement of the small plots in this figure roughly corresponds to the arrangement of the dots in Fig. 7. Cases with light gray background are stable with respect to CTEI, according to the RD criterion.

investigated the decoupling of a cloud-topped boundary layer with mixed layer model, indicate that our cloud layer is not decoupled from the subcloud layer. The GCSS study reported that half of the LESs joined in this intercomparison study exhibit decoupling. The vertical velocity variance has a maximum in the cloud layer and a second at the 400-m level in the subcloud layer, where the maximum of the third moment of the vertical velocity is found for these hours. The positive third moment suggests that the circulation is updraft dominated, that is, convection is largely driven by surface fluxes.

Our results are generally similar to those of the other models participating in the GCSS study and re-

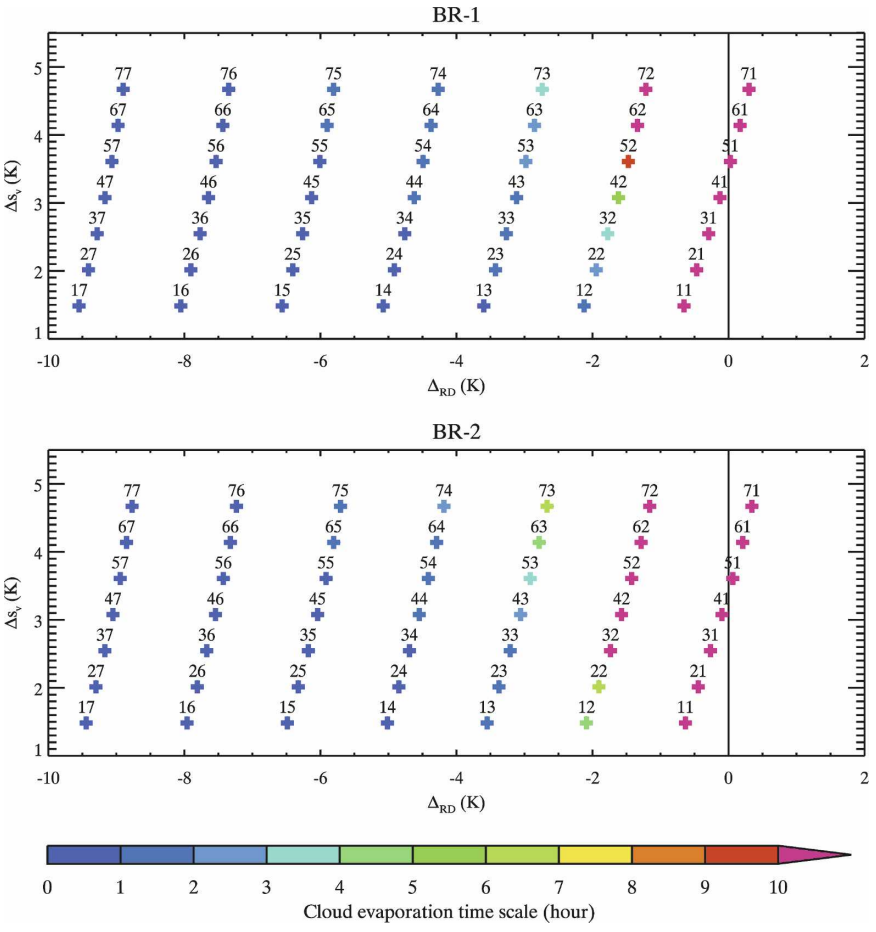

FIG. 10. Same as in Fig. 7 but for BR-1 and BR-2. The stability boundary based on the SB criterion is omitted.

produce the observed fields reasonably well. We conclude that the model is suitable for use in the BR experiments.

3. Results

a. CTEI diagrams

The CTEI diagram for BR-0.5 is shown in Fig. 7. The figure has Δ_{RD} on the horizontal axis and Δs_v on the vertical axis. The figure shows the cloud evaporation time scale, which is defined as the time increment over which the LWP decreases by a factor of e, so that about 63% of the liquid has been evaporated. The SB stability boundary is shown by the dotted line. A diagram modeled after a famous figure of KS for BR-0.5 is presented in Fig. 8. The figure shows the KS ($\kappa = 0.27$, equivalent to the RD criterion; see appendix A) and MM ($\kappa = 0.7$) criteria.

Generally, the cases that are unstable by the RD criterion have cloud evaporation time scales of 2 h or less. The time scale increases as Δ_{RD} (Fig. 7) and $\Delta\theta_e$ (Fig. 8) increase toward the RD boundary. All cloud evaporation time scales for the stable cases (61, 71, 81, and 91) are shown as longer than 10 h, but in reality cloud evaporation does not take place at all. As MB anticipated, the results are not consistent with the SB and MM criteria.

Figure 9 shows examples of the time–height distributions of the cloud fractions for a subset of BR-0.5. For all cases with $\Delta_{RD} > 0$, the clouds maintain 100% cloud cover and keep the same vertical structure for the entire period. In the runs for which $\Delta_{RD} < 0$, most of the cases show changes in the vertical structure due to evaporatively driven entrainment, which is the only process driving turbulence in the model. Complete cloud dissipation within several hours occurs for more than half of the unstable cases, and most of the cloud dissipation cases experience "rapid" cloud breakup with the cloud evaporation time scale of 1 h. For the cases with the cloud evaporation time scale of 2 h, over

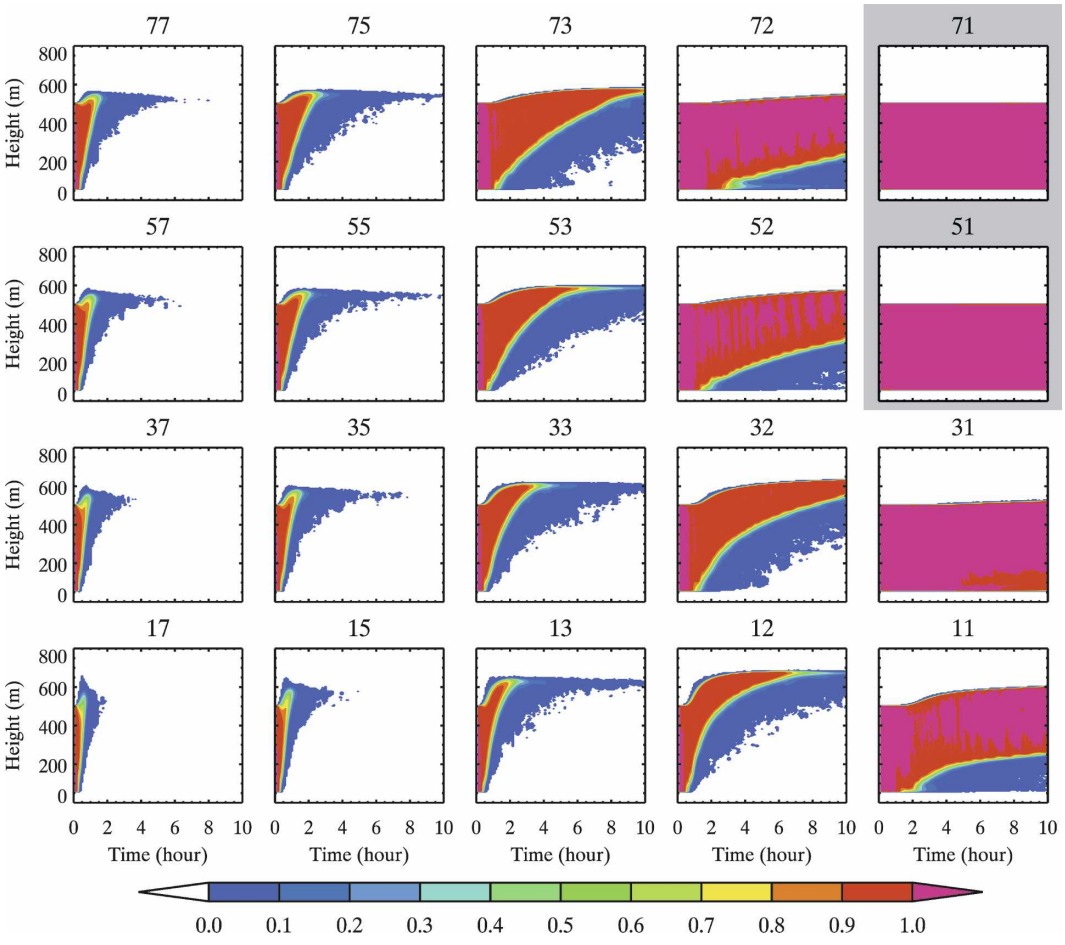

FIG. 11. Same as in Fig. 9 but for BR-1. The initial Δs_v and Δ_{RD} of each case are omitted.

90% of the LWP is evaporated (not shown). Near the boundary on the unstable side, the clouds remain unbroken; nevertheless, cloud thinning takes place with the cloud base rising faster than the cloud top. The cloud thinning would perhaps result in complete cloud dissipation with a longer simulation time. The figure also suggests that a stronger inversion resists cloud breakup with negatively larger Δ_{RD}. For instance, cases 32 ($\Delta_{RD} = -1.79$ and $\Delta s_v = 2.54$) and 95 ($\Delta_{RD} = -5.61$ and $\Delta s_v = 8.91$) have similar cloud breakup scenarios. Thus, both Δ_{RD} and Δs_v may have physical significance for the speed of cloud breakup.

The CTEI diagrams for BR-1 and BR-2 are presented in Fig. 10. The cloud evaporation time scales are less than 2 h for about two-thirds of the unstable cases. Like BR-0.5, the time scale increases as Δ_{RD} increases toward zero. Corresponding time–height distributions of the cloud fraction for the subset of BR-1 are shown in Fig. 11. As in BR-0.5, rapid cloud breakup happens in most of the unstable cases, and rapid cloud-top ascent also occurs; the cloud tops of BR-1 rise by more than 100 m, and those of BR-2 (not shown) by more than 200 m, over the first couple of hours.

b. *How strong is the positive feedback?*

The BR experiments produce cloud breakup, which is in many cases rapid. The CTEI hypothesis predicts cloud breakup as a secondary effect with strong TKE production through rapid entrainment associated with buoyancy reversal. Moeng (2000) did not obtain rapid entrainment and strong TKE production in her LESs. In the following discussion, we explore these issues with case 73 for each of the three series. The runs studied are referred to as BR-0.5-73, BR-1-73, and BR-2-73.

Two movies of BR-0.5-73 are provided to aid in understanding our results. They are available as supplemental material at http://dx.doi.org/10.1175/JAS2438.s1. Figure 12 shows some snapshots from these movies. Figure 12a shows the negative (positive) buoyancy colored red (white), and Fig. 12b shows the cloud water. The left panels show the first negatively buoyant thermal falling away from the cloud top, leaving the nega-

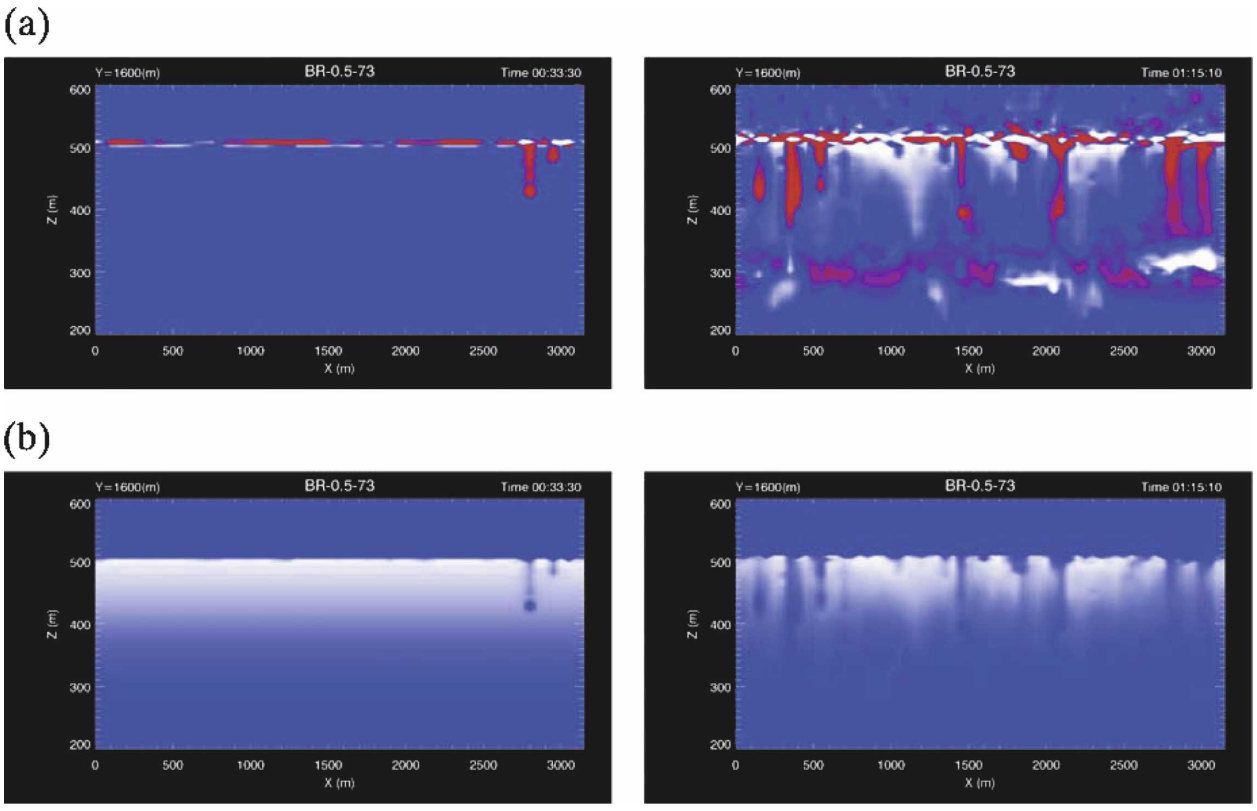

FIG. 12. Snapshots of the BR-0.5-73 movies available at http://dx.doi.org/10.1175/JAS2438.s1. (a) A cross-sectional view of the departure from the horizontal average over the domain of the virtual dry static energy, i.e., buoyancy. Negative buoyancy less than −0.1 K is colored red, and positive buoyancy more than 0.1 K is colored white. Between −0.1 and 0.1 K, a color gradation is used with blue as the center color. (b) A cross-sectional view of the cloud water. White represents maximum liquid water mixing ratio found anywhere in the domain at any time during the simulation, and blue represents clear air. The left slides are at the time when the first negatively buoyant thermal is moving downward from the cloud top, and the right slides are at the time when the vertically integrated TKE becomes maximum.

tive buoyancy and dry air above. The right panels show snapshots near the time when the vertically integrated TKE reaches its maximum. The cloud water field looks like rain dripping down a window pane. The buoyancy field has narrow downdrafts and wide updrafts. Thermals acquire positive buoyancy near the cloud base and overshoot. They do not penetrate below $z = 200$ m.

Figure 13 shows the time series of LWP normalized by the initial value. The figure suggests a cloud evaporation time scale of about 100 min for BR-0.5-73, 210 min for BR-1-73, and 400 min for BR-2-73. The estimated cloud evaporation speed, which is defined as the ratio of 67% of the initial LWP (i.e., 62 g m^{-2} for BR-0.5-73, 254 g m^{-2} for BR-1-73, and 835 g m^{-2} for BR-2-73) to the cloud evaporation time scale, is 0.007 g m^{-2} s^{-1} for BR-0.5-73, 0.014 g m^{-2} s^{-1} for BR-1-73, and 0.023 g m^{-2} s^{-1} for BR-2-73. Thus, the cloud evaporates faster when the initial cloud water amount is larger.

Figure 13 also suggests that entrainment and TKE spontaneously develop in the presence of buoyancy reversal. The magnitudes of both variables increase with the cloud-top liquid water mixing ratio (i.e., 0.5 g kg^{-1} for BR-0.5, 1 g kg^{-1} for BR-1, and 2 g kg^{-1} for BR-2); for a given value of Δ_{RD}, a cloud with a larger liquid water amount experiences more rapid entrainment and stronger TKE. These results support the APS hypothesis that the strength of CTEI is sensitive to the liquid water amount.

The entrainment rate and the vertically integrated TKE have similar time evolutions; the two variables increase to maxima then decrease. The unstable cases show cloud drying and then breakup immediately after each simulation starts, and the strength of the entrainment reaches its maximum at an early stage of the simulation. In CTEI, entrainment consumes cloud water to generate convection, so the feedback must die away when the supply of cloud water has been depleted. The TKE therefore decreases, as does the entrainment rate.

The initial LWP and cloud thickness of BR-0.5-73

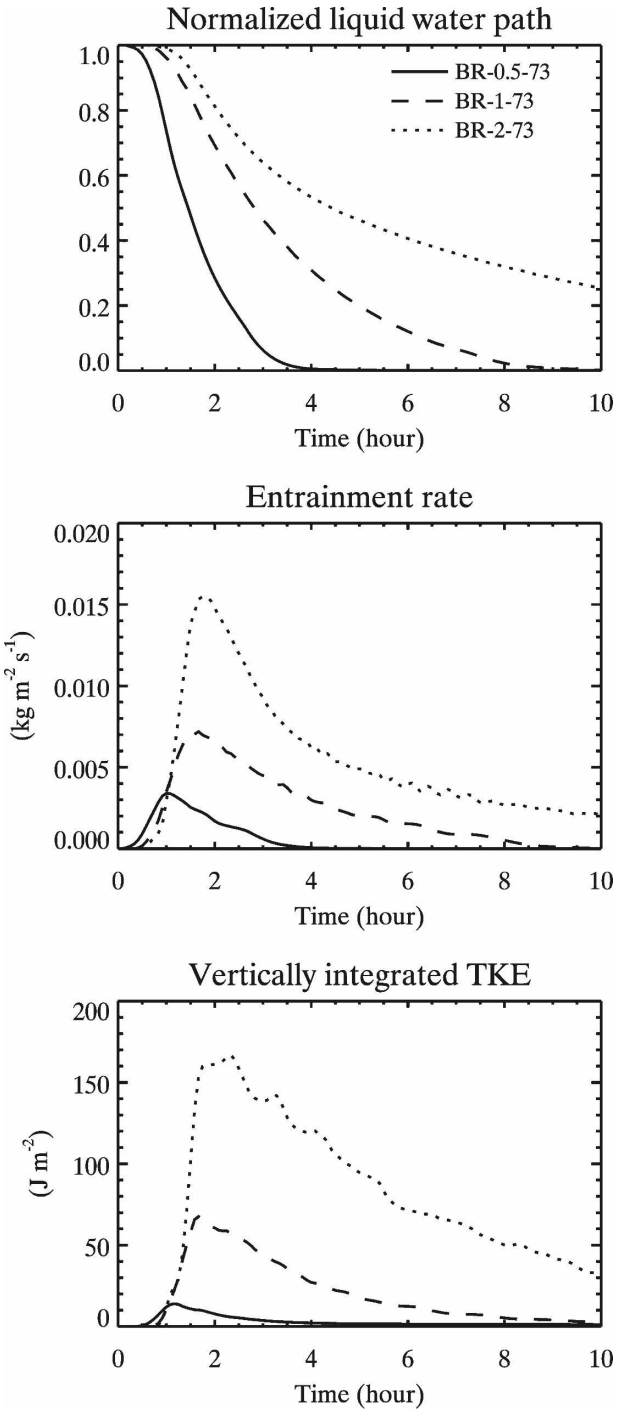

FIG. 13. Time evolution of normalized liquid water path, entrainment rate, and vertically integrated TKE for case 73 of BR-0.5, BR-1, and BR-2. The entrainment rate is smoothed with a 30-min running mean.

are close to those of DYCOMS-II. The DYCOMS-II PBL is unstable with respect to CTEI, and it is deeper than BR-0.5-73. The GCSS DYCOMS-II case includes the surface fluxes as well as the longwave radiation, both of which promote convection. The vertically integrated TKE of DYCOMS-II (Fig. 5) is about 20 times larger than that of BR-0.5-73 (Fig. 13). Moreover, for the entire BR-0.5 series, the largest value of the vertically integrated TKE is less than 20% of that in DYCOMS-II (not shown), and the cases at the bottom-left corner of the CTEI diagram (Fig. 7) have larger TKEs than those at the upper right. We conclude that the turbulence produced by CTEI is weak compared to that typically found in marine stratocumulus clouds. Moeng (2000) did not observe large TKE with $\Delta_{RD} < 0$. The maximum liquid water mixing ratios of the CTEI unstable cases among her LESs are between 0.03 and 0.22, less than 0.5 g kg^{-1}. Her results are consistent with ours.

c. What processes can mask CTEI?

According to MB and Moeng (2000), as well as our BR experiments, spontaneous entrainment happens if and only if the RD criterion is satisfied, and CTEI forces the cloud toward dissipation if no other processes are active. The BR experiments show that the positive feedback is weak, so that in realistic cases, with many active processes, CTEI may not be strong enough to control the state of the marine boundary layer. Persistent solid cloud decks subject to CTEI have been observed and simulated in earlier studies. We therefore hypothesize that CTEI can be masked by sufficiently strong cloud-building processes (CBPs), for example, radiative cooling and surface evaporation. Cloud dissipation due to CTEI is expected only when CTEI can overcome the CBPs. This may rarely happen.

We now discuss a few tests of the CTEI–CBP hypothesis; more should be examined in the future. The marine stratocumulus-topped PBL has two coexisting types of convection: convection from the cloud top, forced by radiative cooling, and convection from the lower boundary, forced by surface sensible and latent heat fluxes. For marine stratocumulus clouds, the radiative cooling and surface latent heat flux cool the layer and supply moisture from the surface, thus favoring continued cloudiness. To see the effects of these two processes on a cloud field subject to CTEI, three additional LESs based on BR-0.5-73 were performed. The first, called RAD, is BR-0.5-73 but with longwave radiation. The SST is assumed to be equal to the temperature at the lowest model level. The second, LHF100, is BR-0.5-73 but with a prescribed constant surface latent heat flux of 100 W m^{-2}. The third, RAD-LHF100, has both longwave radiation and a prescribed surface latent heat flux of 100 W m^{-2}. In these experiments, the longwave radiation and/or the latent heat

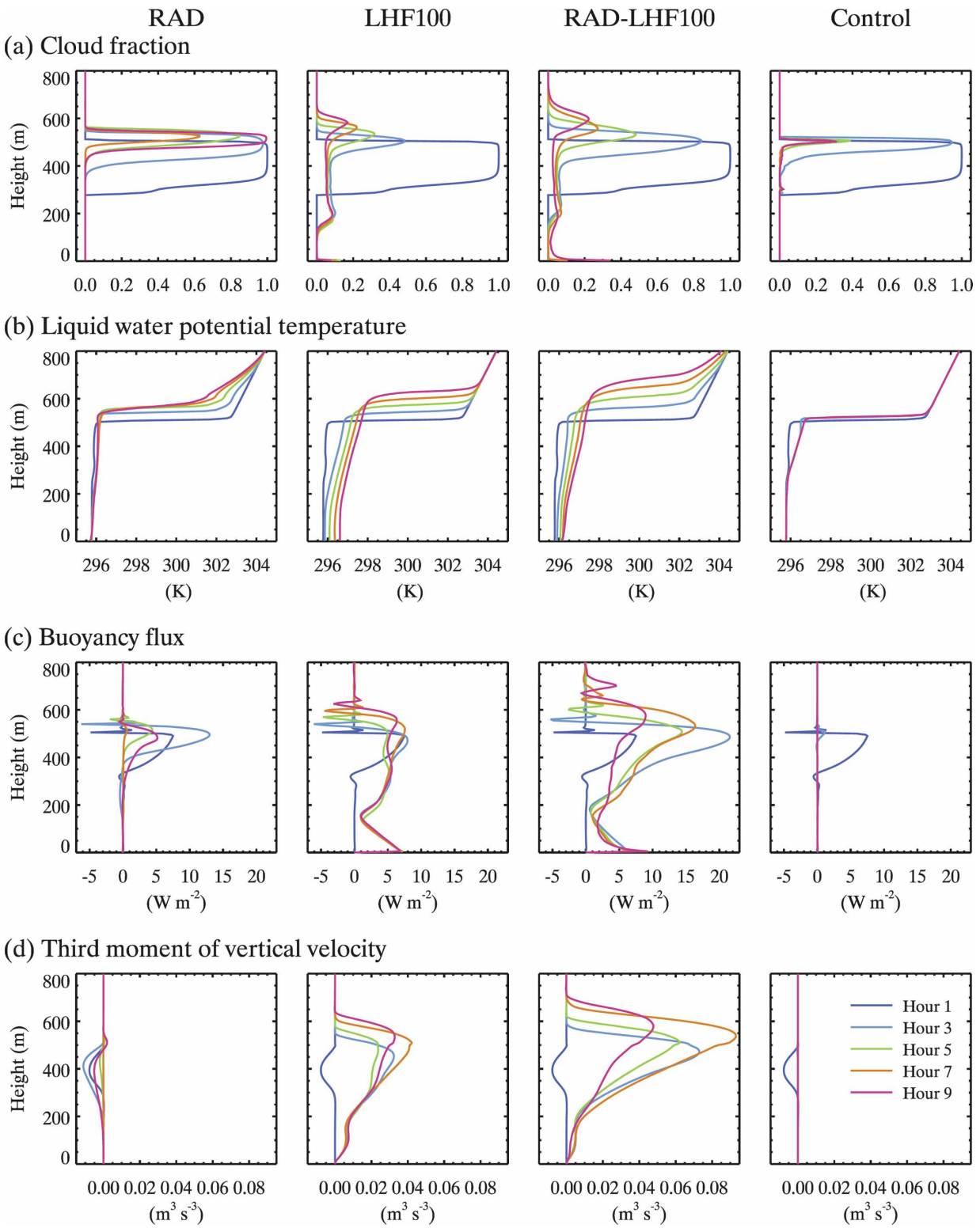

FIG. 14. Vertical profiles of the cloud fraction, liquid water potential temperature, buoyancy flux, and third moment of vertical velocity for RAD, LHF100, and RAD-LHF100, at 2-h intervals starting from hour 1. BR-0.5-73 is also shown and is labeled as Control. Because CBPs are introduced at hour 1, the profile shown for hour 1 is the same as that of BR-0.5-73.

flux are introduced after 1 h of simulated time, when the CTEI-induced convection is already established. The surface sensible heat flux was set to zero in all of the runs.

Figure 14 shows the vertical profiles of the cloud fraction, liquid water potential temperature, $\theta_l = \theta - [(L/c_p)(\theta/T)]l$, buoyancy flux, and third moment of the vertical velocity for RAD, LHF100, and RAD-LHF100 as well as BR-0.5-73 labeled as Control. The profiles for hour 1 are the same as that of Control. The cloudiness of Control quickly decreases, and the turbulent activity almost ceases by hour 3. The downdrafts are more intense than the updrafts so that the third moment of the vertical velocity is negative in the cloud layer at hour 1 as expected for CTEI. The liquid water potential temperature becomes warm, that is, less mixed, in the cloud layer.

In RAD, the cloudiness decreases to less than 0.8 by hour 7, but then increases by hour 9. The profiles of the buoyancy flux show weakening turbulence, and the profile for hour 7 has almost no flux. Perhaps, cloud evaporation due to CTEI is almost terminated at this time because of the depletion of the cloud water. Radiative cooling keeps the liquid water potential temperature profile same all the time and should allow the cloud to reform. The RD criterion for instability is satisfied at hour 9, so that the reborn cloud starts to break up (not shown).

The surface latent heat flux produces a cumulus like condition in LHF100. The cloudiness decreases to 0.5 at hour 3 and continues decreasing. The PBL becomes unmixed so that the profiles of the liquid water potential temperature become a cumulus type from a stratocumulus type. The third moment of the vertical velocity suggests that the circulation rapidly shifts from downdraft dominated to updraft dominated. The buoyancy flux profiles show strengthening turbulence in the cloud layer, and the vertical gradient in the subcloud layer is negative upward, which is similar to that of realistic clouds.

For RAD-LHF100, the boundary layer condition also becomes cumulus type with stronger turbulence as a result of a coupling of radiation and surface latent heat flux. The entrainment rate and vertically integrated TKE are strongest in RAD-LHF100 (Fig. 15). The cloud should experience more evaporation because of this increased entrainment. With a reduced cloud fraction, the radiative cooling produces less chilling. Even with transported moisture from the surface, the cloudiness of RAD-LHF100 decreases faster than in RAD.

Normalized LWPs shown in Fig. 15 suggest that the cloud evaporation time scale for LHF100 is about 100 min, which is the same as that of Control. The time scales for RAD and RAD-LHF100 are about 135 min, which would be longer if the longwave radiation had been introduced at the beginning of the simulation. The radiative cooling makes CTEI slow down, but the latent

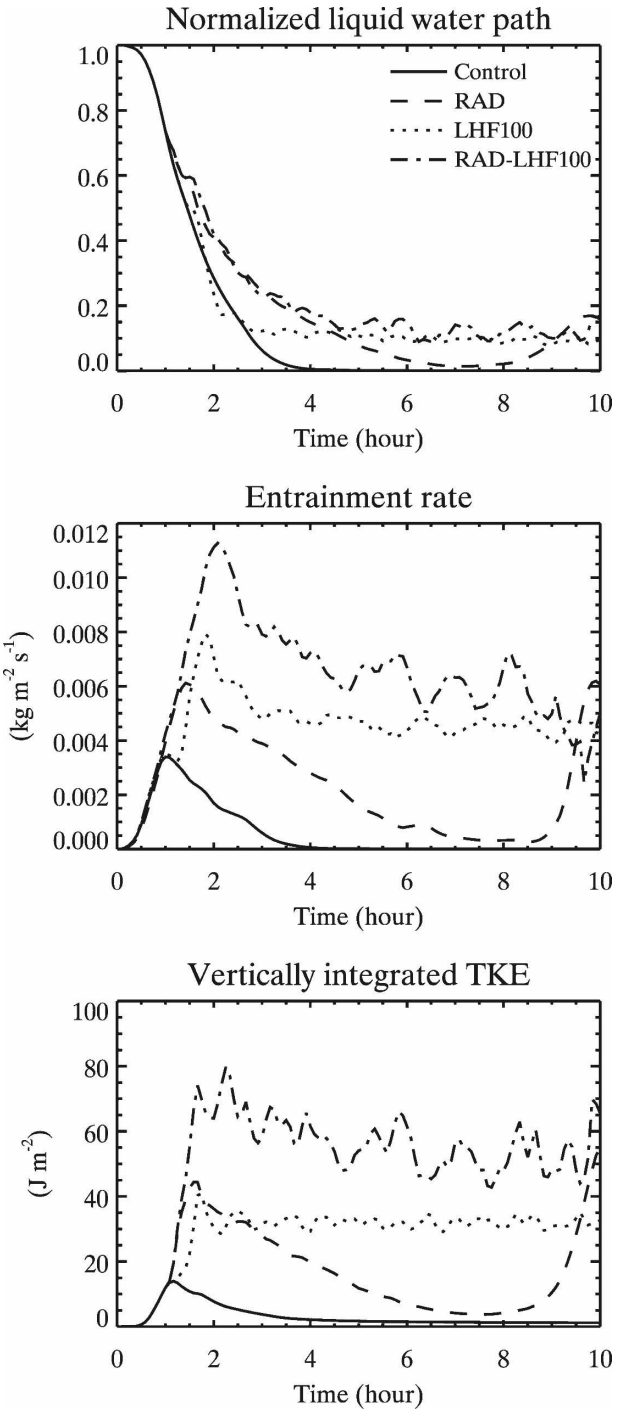

FIG. 15. Same as in Fig. 13 but for RAD, LHF100, and RAD-LHF100. BR-0.5-73 is also shown and is labeled as Control.

heat flux does not. That is, radiative cooling counteracts CTEI more effectively than the surface latent heat flux.

These results show that radiative cooling has a potential to overcome CTEI. This can explain the persistent cloud decks observed under CTEI conditions. The negative feedback proposed by Moeng et al. (1995) may play a role here.

d. Decoupling

As discussed in section 2e, decoupling has been hypothesized as a cloud breakup mechanism for marine stratocumulus clouds (e.g., Bretherton and Wyant 1997). A decoupled PBL has distinct turbulent circulations in the cloud and subcloud layers. Between the two layers, a negative buoyancy flux inhibits communication.

The PBLs of the BR experiments are not expected to be decoupled according to the buoyancy integral ratio discussed by Turton and Nicholls (1987) and Bretherton and Wyant (1997). However, as discussed in section 3b, the downdraft thermals do not penetrate below $z =$ 200 m. The buoyancy flux and the third moment of the vertical velocity for BR-0.5-73 (Fig. 14) are zero below the cloud base, suggesting that the convection is confined within the initial cloud layer, and no turbulence exists in the subcloud layer. In this sense, the PBL is decoupled in the BR experiments.

4. Summary and conclusions

We have used LES to explore CTEI through idealized buoyancy reversal experiments, following MB. The BR experiments clearly show the hypothesized CTEI positive feedback. Spontaneous entrainment develops through buoyancy reversal, if and only if the cloud top is unstable by the RD criterion. In our idealized experiments, the CTEI-driven entrainment eventually destroys the uniform cloud. The rate of cloud destruction depends on Δs_v and $(\Delta s_v)_{\text{crit}}$. The experiments affirm the prediction of APS that the strength of the evaporatively driven turbulence depends on the cloud-top liquid water mixing ratio; larger cloud water leads to stronger feedback. Comparison with a realistic marine stratocumulus LES suggests that the feedback is usually weak for marine stratocumulus clouds because of their small liquid water amounts.

Additional LESs, which have longwave radiation, surface latent heat flux, or both, were performed to see how effectively CBPs can work against CTEI. Radiative cooling decelerates cloud destruction and indicates a capability to mask CTEI. On the other hand, prescribed surface latent heat flux drives the system toward cumulus convection. Since these two processes should be effectively coupled for steady clouds, thus cloud breakup occurs if and when CTEI overwhelms the CBPs. Observations of persistent stratocumulus clouds under CTEI conditions can be understood if CBPs mask the effects of CTEI.

All of our LESs were performed using a small horizontal domain (i.e., about 3 km on a side) with periodic lateral boundary conditions. Thus, none of our LESs has mesoscale circulations, for example, closed cells. We speculate that CTEI might play a role around the edges of closed cellular circulations, where the clouds are broken. For example, entrained air may drift horizontally some distance before buoyancy reversal happens. To evaluate the possible role of CTEI in mesoscale circulations, an LES with roughly a 100-km horizontal domain size would be required.

Although there are still many uncertainties, it is reasonable to define CTEI as spontaneous entrainment associated with buoyancy reversal, without mentioning cloud destruction. Since the positive feedback of CTEI is weak, cloud breakup is not expected when the clouds are strongly maintained by other processes.

Further study, with a different experimental design, is needed to understand the effects of CTEI on the structure of the marine layer as it evolves downstream through the trade wind region (Moeng and Arakawa 1980).

Acknowledgments. This research has been supported by NASA Contract NNL04AA36G, NSF ATM-0415184, DOE ARM DE-FG02-02ER63370, and DOE Cooperative Agreement DE-FG02-01ER63163. We thank Douglas Lilly and Wayne Schubert for helpful comments.

APPENDIX A

Summary of CTEI Criteria

Table 2 lists six CTEI criteria. The RD and KS criteria are actually the same; their equivalency can be shown in the following way: the KS instability criterion is

$$\Delta\theta_e < \kappa\left(\frac{L}{c_p}\right)\Delta r, \tag{A1}$$

where

$$\kappa = \frac{(1+\gamma_\theta)\dfrac{c_p}{L}\theta_0}{1+(1+\delta)\gamma_\theta\dfrac{c_p}{L}\theta_0}. \tag{A2}$$

Here $\gamma_\theta = (L/c_p)\,(\partial q^*/\partial\theta)_p$ and θ_0 is a reference potential temperature. If we assume $T \cong \theta$, then

$$\kappa = \frac{(1+\gamma)\dfrac{c_p}{L}T_0}{1+(1+\delta)\gamma\dfrac{c_p}{L}T_0} \simeq \frac{\epsilon}{\beta}, \tag{A3}$$

where β is defined by Randall (1980) as

$$\beta \equiv \frac{1+(1+\delta)\gamma\epsilon}{1+\gamma}. \tag{A4}$$

With (A3) and $\theta_e \simeq \theta + (L/c_p)q$, (A1) can be approximately expressed in terms of moist static energy instead of equivalent potential temperature as

$$\beta\Delta h - \epsilon L\Delta r < 0. \tag{A5}$$

This is the RD criterion. A more detailed discussion of the relationship between the RD criterion and the KS criterion is given by Shao et al. (1997).

We find that $\kappa \simeq 0.27$ is the stability boundary of the KS criterion for BR-0.5, if κ is calculated with the values at level B, that is, $\theta_0 = \theta_B$, $\gamma_\theta = \gamma_{\theta_B}$ in (A2). Although $\kappa = 0.23$ has been widely used, Fig. A1 shows that κ is a weak function of pressure below 900 hPa and a stronger function of temperature. For this reason, using a single value of κ as a stability boundary is not possible if PBLs of various temperatures are considered. Moreover, including the effects of the inversion air will bring further complications. Since the BR experiments use a single PBL sounding for each series, and κ is evaluated at level B, we have one KS stability boundary for each series. Cases 82 and 92 are both shown as unstable in Fig. 7 but stable in Fig. 8. This is caused by the use of the temperature at the level B only for κ, more specifically constant γ_θ, to obtain a single stability boundary for the KS criterion.

SB proposed a stability parameter D that is the ratio of minimum buoyancy reduction to inversion strength:

$$D \equiv -\left[\frac{(s_v)_{\text{at }\chi^*} - (s_v)_B}{\Delta s_v}\right] = \frac{\dfrac{(\Delta s_v)_{\text{crit}}}{\Delta s_v} - 1}{1 + \dfrac{(\Delta s_v)_{\text{crit}}}{[1-(1+\delta)\epsilon]Ll_B}}. \tag{A6}$$

The second equality in (A6) was derived by Shao et al. (1997). Because $1 + \{(\Delta s_v)_{\text{crit}}/[1-(1+\delta)\epsilon]Ll_B\}$ is positive, the sign of D is determined by the sign of $[(\Delta s_v)_{\text{crit}}/\Delta s_v] - 1$, and so D is positive when Δ_{RD} is negative. The relationship between Δ_{RD} and Δs_v can be obtained from (1) and (A6):

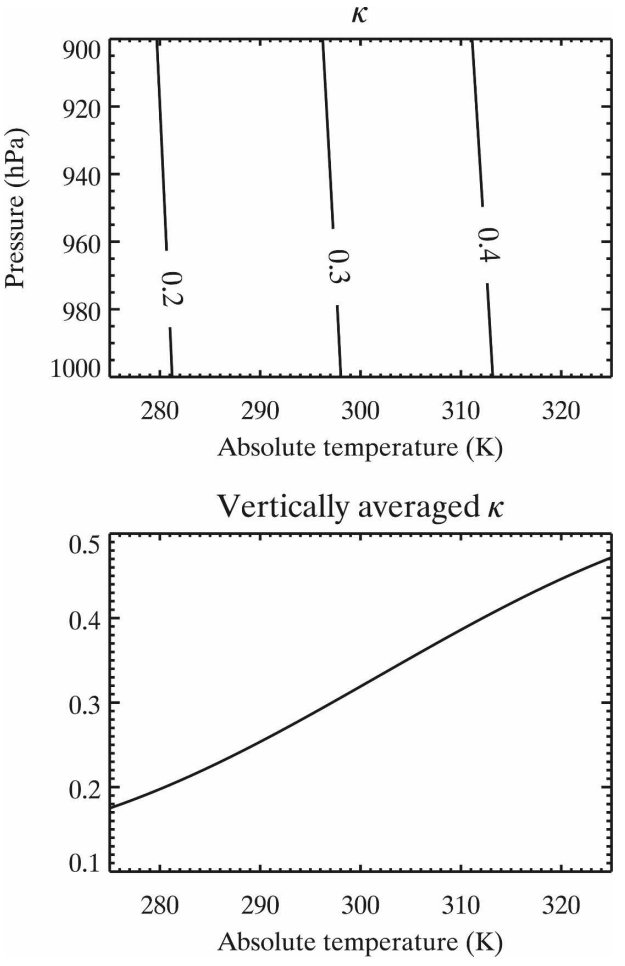

FIG. A1. Stability parameter κ and its vertically averaged value between 1000 and 900 hPa. Here κ is computed by (A2) with temperature and pressure as input.

$$\Delta_{\text{RD}} = \frac{\Delta s_v + [1-(1+\delta)\epsilon]Ll_B}{D\Delta s_v - [1-(1+\delta)\epsilon]Ll_B} D\Delta s_v. \tag{A7}$$

Based on laboratory experiments and numerical studies performed by Shy and Breidenthal (1990), SB proposed that CTEI occurs for

$$D > 1.3. \tag{A8}$$

A value of D of order 1 means that $(s_v)_{\text{at }\chi^*} - (s_v)_B$ is comparable to the strength of the inversion, that is, evaporative cooling is capable of chilling air from above the inversion until its temperature is comparable to that of the cloud layer. For stratocumulus conditions, (A8) could mean a chilling of 10 K or more, which is out of the question with stratocumulus liquid water mixing ratios. We comment that such extreme chilling is not required for the production of negatively buoyant parcels. Since $D > 0$ corresponds to the RD criterion, the

SB criterion is much more difficult to satisfy. For $0 < D < 1.3$, SB suggested that there is evaporative enhancement of entrainment, instead of the hypothesized explosive positive feedback of CTEI.

MM derived an instability criterion by considering the conversion of potential energy to kinetic energy between unsaturated upper layer and saturated lower layer. Their criterion for instability is given by

$$\kappa > 0.7. \tag{A9}$$

MM also showed that their criterion reduces to the KS criterion if both layers are saturated. MM demonstrated how their criterion works with a diagram similar to KS with available observational data in terms of fractional cloudiness.

Duynkerke (1993) proposed that CTEI occurs if

$$\Delta_a = \int_0^1 \frac{(\theta_v)_{\text{mix}} - (\theta_v)_B}{1 - \chi}\, d\chi < 0. \tag{A10}$$

He showed that as the liquid water content of a cloud increases from zero, the criterion changes gradually from the dry-adiabatic criterion (i.e., $\Delta s_v < 0$) to the RD criterion or "wet-adiabatic criterion" with increasing liquid water amount. He argued that other criteria are just simplification of his criterion.

Lilly (2002) first developed a new entrainment parameterization and then derived a CTEI criterion for which his entrainment parameterization gives an infinite entrainment rate:

$$-\frac{L\Delta r}{c_p \Delta\theta_l} > \kappa_L \gtrsim 1.28. \tag{A11}$$

Here θ_l is the liquid water potential temperature, and $\kappa_L \approx 1.28$ is equivalent to the RD criterion. Assuming $T \cong \theta$ and using the definitions of θ_l and θ_e, the relationship between κ and κ_L can be derived as

$$\kappa = 1 - \frac{1}{\kappa_L}. \tag{A12}$$

The value of κ_L decreases as cloud-base height decreases and as cloud-top wetness increases. Lilly's criterion becomes equivalent to the RD criterion when the cloud-base height becomes zero and the cloud-top wetness becomes 100%. The cloud-top wetness is defined in terms of saturated and unsaturated buoyancy fluxes. He suggested that for real situations, κ_L takes a larger value, for example, $\kappa_L = 2.55$ (or $\kappa \cong 0.6$) with typical cloud-base height and cloud-top wetness.

APPENDIX B

List of Abbreviations

Table B1 shows the list of the abbreviations that are used repeatedly throughout the text and whose meaning may not be obvious. They are mostly related to the proposed CTEI criteria and simulation case names.

TABLE B1. List of abbreviations.

Abbreviation	Origin and reference
RD	Randall (1976, 1980); Deardorff (1980)
KS	Kuo and Schubert (1988)
APS	Albrecht et al. (1985)
SB	Siems et al. (1998)
MM	MacVean and Mason (1990)
MB	MacVean and Bretherton (1999, unpublished manuscript)
BR	Buoyancy reversal
BR-#	BR experiment with the # g kg^{-1} cloud-top liquid water mixing ratio
BR-#-##	Case ## of BR-#
CBP	Cloud-building process
RAD	Case of BR-0.5-73 with the longwave radiation, no surface flux
LHF100	Case of BR-0.5-73 with the constant surface latent heat flux of 100 W m^{-2}
RAD-LHF100	Case of BR-0.5-73 with the longwave radiation and the constant surface latent heat flux of 100 W m^{-2}

APPENDIX C

Soundings for BR-0.5, BR-1, and BR-2

One baseline sounding, that is, BR-0.5 with index 11 in Fig. 3, is based on case K of MB. The mixed layer and the tropospheric sounding are indicated in Table C1. Without changing the mixed layer sounding, 63 different free tropospheric soundings of BR-0.5 were created by applying different jump values for virtual potential temperature and total water mixing ratio. For BR-1 and BR-2, the mixed layer soundings are generated so as to have the same value of the RD stability parameter, Δ_{RD}, of BR-0.5. All three series have the same free tropospheric soundings for each index.

SAM requires the initial profiles of the liquid water potential temperature and the total water mixing ratio as well as the surface pressure. Level B values are computed by

$$\begin{cases} (\theta_l)_B = \theta_B - \left(\dfrac{L}{c_p}\dfrac{\theta_B}{T_B}\right) l_B \\ r_B = q_B^* + l_B, \end{cases} \tag{C1}$$

where $q_B = q_B^*$.

The surface pressure is obtained by the following method: from the moist static energy and total water mixing ratio, the surface temperature is given as

$$T_S = c_p^{-1}(h_B - Lr_S). \tag{C2}$$

TABLE C1. Sounding information for case K given by MB.

Cloud top	Jump value	Vertical gradient for free troposphere	Cloud base
$z_B \cong 500$ m $p_B = 944$ hPa $T_B = 292.2$ K $\theta_B = 297$ K $l_B = 0.5$ g kg^{-1}	$\Delta\theta_v = 1.51$ K $\Delta r = -2.35$ g kg^{-1}	$d\theta_v/dz = 0.006$ Km^{-1} $dr/dz = 0$ g kg^{-1} m^{-1}	$z_C \cong 280$ m

Following adiabatic lapse rate,

$$T(z) = T_S - \frac{g}{c_p} z. \tag{C3}$$

Using the hydrostatic relationship and equation of state, we get

$$\frac{1}{\rho}\frac{\partial p}{\partial z} = -\frac{g}{RT}. \tag{C4}$$

Substituting (C3) into (C4), integrating with height, and then solving for p_S, we find that

$$p_S = p_B\left(1 - \frac{g}{c_p}\frac{z_B}{T_S}\right)^{-(c_p/R)}. \tag{C5}$$

Free tropospheric soundings are created as follows: for each index of $i = [1, 2, 3, 4, 5, 6, 7, 8, 9]$ and $j = [1, 2, 3, 4, 5, 6, 7]$, which are indices of row and column starting from the bottom right on Fig. 3, jump values of virtual potential temperature and total water mixing ratio are calculated as

$$\begin{cases} \Delta\theta_v = \begin{cases} 1.51 + 0.54(i-1) & \text{for} \quad i \leqq 7 \\ 4.75 + 2.16(i-7) & \text{for} \quad i = 8, 9 \end{cases} \\ \Delta r = -2.35 - 2(j-1). \end{cases} \tag{C6}$$

Here the virtual potential temperature jumps with $i = 8$ and 9 are for the strong inversion strength cases. From $(\theta_v)_B = \theta_B\,(1 + \delta q_B - l_B)$ and r_B, variables at level $B+$ are given as

$$\begin{cases} (\theta_v)_{B+} = (\theta_v)_B + \Delta\theta_v \\ r_{B+} = q_{B+} = r + \Delta r \\ l_{B+} = 0. \end{cases} \tag{C7}$$

Above level $B+$, sounding is simply calculated as

$$\begin{cases} \theta_v(z) = (\theta_v)_B + \dfrac{d\theta_v}{dz}(z - z_{B+}) \\ r(z) = r_{B+} + \dfrac{dr}{dz}(z - z_{B+}) \\ l(z) = 0. \end{cases} \tag{C8}$$

For BR-1 and BR-2, we created the mixed layer soundings so as to have the same Δ_{RD} of BR-0.5. The virtual dry static energy jump is given as

$$\Delta s_v = c_p \Delta T_v + g\Delta z, \tag{C9}$$

where $T_v \equiv T(1 + \delta r - l)$ is virtual temperature and $\Delta z = 5$ m. From (C9) and the definition of Δ_{RD},

$$\begin{aligned}(T_v)_B &= (T_v)_{B+} - c_p^{-1}[\Delta_{\mathrm{RD}} + (\Delta s_v)_{\mathrm{crit}} - g\Delta z] \\ &= f[(T_v)_{B+}, q^*_{B+}, q_{B+}].\end{aligned} \tag{C10}$$

Thus, the same Δ_{RD} for all three series means the same $(T_v)_B$ for all three series if the sounding of the free troposphere is the same for all three.

To find a suitable $(T_v)_B$, an iterative method is used; warm the absolute temperature with small increments and then assign the saturation mixing ratio calculated with the new temperature as the new water vapor mixing ratio. With the specified liquid water mixing ratio, that is, 1 g kg^{-1} for BR-1 and 2 g kg^{-1} for BR-2, a new virtual temperature is calculated. This cycle is continued until the new virtual temperature is close enough to the virtual temperature at level B of BR-0.5.

APPENDIX D

Test of the Sensitivity to Grid Spacing with DYCOMS-II Simulations

To perform a large number of LESs of the BR experiments with the available computing power, we first simulated with GCSS DYCOMS-II with three combinations of the horizontal and vertical grid spacings: grid A is $\Delta x = 35$ and $\Delta z = 5$ m, grid B is $\Delta x = 50$ and $\Delta z = 5$ m, and grid C is $\Delta x = 50$ and $\Delta z = 10$ m. Grid A was used in the GCSS study (Stevens et al. 2005). Grid B is less isotropic than grid A and has a coarser horizontal grid spacing. Isotropic grid has the same grid spacing in all directions. Grid C is more isotropic than grid A and has coarser horizontal and vertical grid spacings. Isotropy may be important, especially where quasi-isotropic small-scale processes are as important as larger-scale processes. For the same time step, grid B is about 2 times faster than grid A, and grid C is about

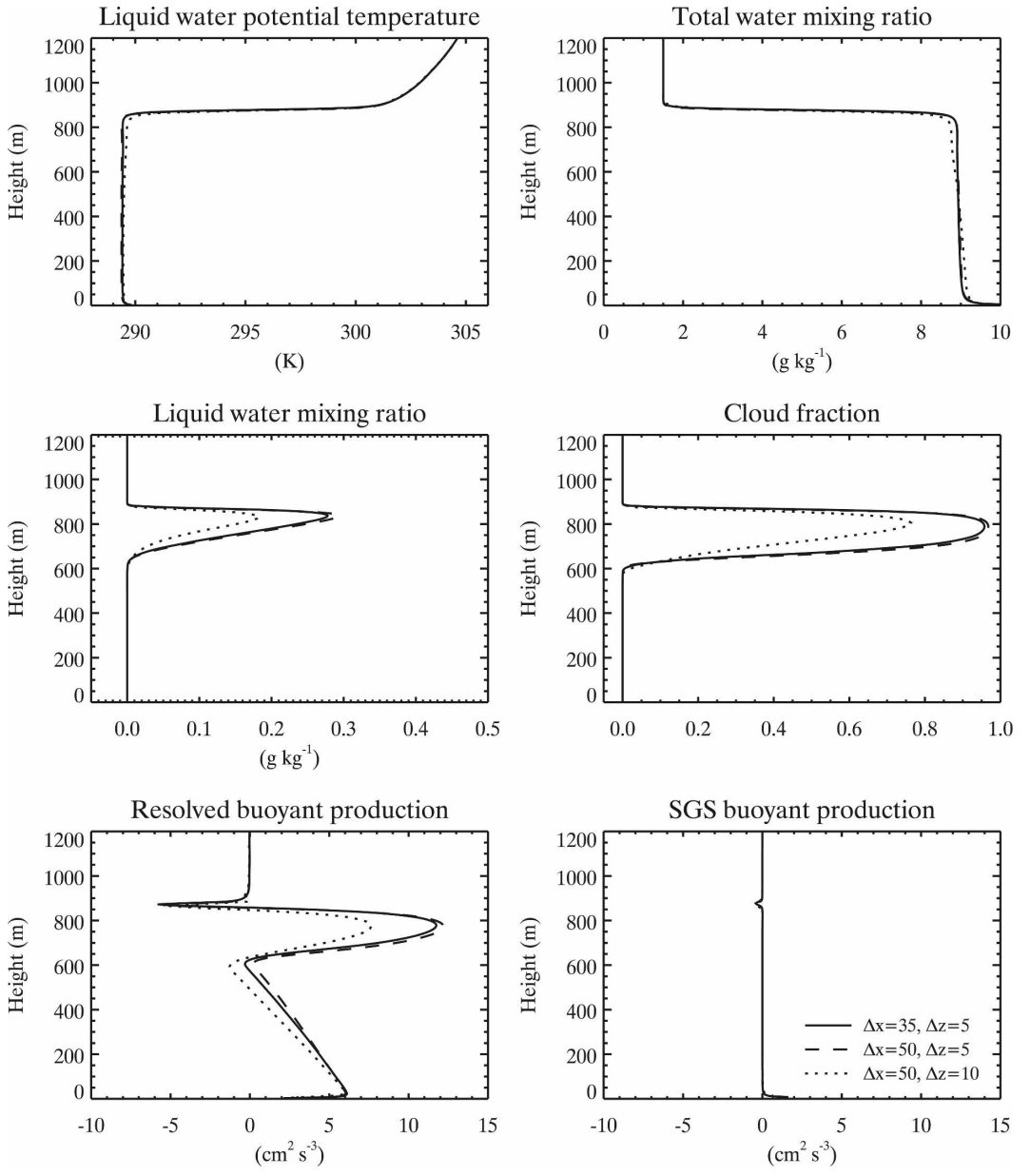

FIG. D1. One-hour-averaged vertical profiles at hour 4 for three different combinations of horizontal and vertical resolutions. Liquid water potential temperature, total water mixing ratio, liquid water mixing ratio, cloud fraction, and resolved and SGS buoyant production of TKE are presented.

4 times faster than grid A. Sensitivity of the entrainment rate to vertical resolution and SGS mixing have been reported (e.g., Bretherton et al. 1999; Stevens et al. 2005). From this point of view, grid A would be the best choice. On the other hand, the BR experiments run faster with grids B and C.

All grids used the same model configuration of Stevens et al. (2005). The simulation with grid A is the same run presented in section 2e. The results for different grid spacings are presented in Fig. D1. All three cases have almost the same profiles of liquid water potential temperature and total water mixing ratio. However, the liquid water mixing ratio and resolved buoyant production in cloud are much smaller for grid C, and according to the cloud fraction, cloud breakup has already taken place. The cloud fraction of grid C drops less than 0.8 after 2 h (not shown), and this breakup is caused not by CTEI but by coarse vertical resolution. On the other hand, grid B has slightly larger liquid water amount and resolved buoyant production in

cloud, and the cloud fraction is close to unity. SGS buoyant production of grids B and C is as small as grid A. This is also true for the resolved TKE and SGS TKE. Since the only TKE source is buoyant production for the BR experiments, these results suggest that grid B can produce a reasonable result compared with the result obtained from grid A, even though grid B is less isotropic. Comparison of the time series of LWP, vertically integrated TKE, and cloud fraction of grid A presented in Fig. 5 and grid B (not shown) also suggests that the effect of reduced isotropy by horizontal resolution is very small for these two grid spacings. Thus, we selected grid B, that is, 5-m vertical and 50-m horizontal grid spacing.

APPENDIX E

A Method to Determine E, z_{B+}, and z_B

To the best of our knowledge, there is no well-developed method for any type of PBL to determine the inversion height, mixed layer depth, or the entrainment rate. We have created a new method, which can apply to dry and stratocumulus-topped boundary layers, as explained below.

From mixed layer theory, the inversion-layer budget equation for the liquid water static energy, $s_l \equiv c_p T - Ll + gz$, is

$$E\Delta s_l + (F_{s_l})_B - \Delta R = 0, \tag{E1}$$

where E is the entrainment rate, F is the vertical flux of subscript variable, and R is the radiative flux. Keeping the assumption of a thin inversion layer, that is, zero storage, but allowing nonzero fluxes at level $B+$, we generalize (E1) to

$$E\Delta s_l - \Delta F_{s_l} - \Delta R \equiv \epsilon_{s_l} = 0. \tag{E2}$$

In reality or LES, there is small but finite storage, ϵ, so generally

$$\epsilon_{s_l} \neq 0. \tag{E3}$$

Similarly, for the total mixing ratio,

$$E\Delta r - \Delta F_r \equiv \frac{\epsilon_r}{L} \neq 0. \tag{E4}$$

We define the total residual from the zero storage assumption as a quadratic function of E, according to

$$\epsilon^2 \equiv \epsilon_{s_l}^2 + \epsilon_r^2 = c_2E^2 + c_1E + c_0, \tag{E5}$$

where

$$\begin{cases} c_2 = (\Delta s_l)^2 + (L\Delta r)^2 \\ c_1 = -2[\Delta s_l(\Delta F_{s_l} + \Delta R) + L^2\Delta r\Delta F_r] \\ c_0 = (\Delta F_{s_l} + \Delta R)^2 + (L\Delta F_r)^2. \end{cases} \tag{E6}$$

It can be shown that $c_1^2 - 4c_2c_0 \leq 0$ and $c_2 > 0$. It follows that the entrainment rate that minimizes ϵ^2 is

$$E = -\frac{c_1}{2c_2}. \tag{E7}$$

The entrainment rate given by (E7), with reasonable levels B and $B+$, is optimally consistent with the mixed layer theory in the sense that the total residual is minimized.

However, we have to find levels $B+$ and B. Searching from the domain top, we locate level $B+$ as the lowest level where both

$$|F_{s_l}| < 0.025|\max(F_{s_l})| \quad \text{and} \quad |F_r| < 0.025|\max(F_r)| \tag{E8}$$

are satisfied. This condition forces near-zero fluxes at level $B+$. Figure E1 shows an example at hour 10 of the DYCOMS-II simulation, with $\Delta x = 35$ and $\Delta z = 5$ m. From Figs. E1a and E1b, we see that the diagnosed level $B+$ is reasonable, and the magnitudes of the residuals are very small in the inversion, due to small coefficients, c_2, c_1, and c_0 (i.e., small Δs_l, Δr, and ΔF).

To determine level B, we introduce the following ratio:

$$\phi \equiv \frac{|\epsilon_{s_l}| + |\epsilon_r|}{|E\Delta s_l| + |\Delta F_{s_l}| + |\Delta R| + |EL\Delta r| + |L\Delta F_r|}. \tag{E9}$$

This is the ratio of the sum of the absolute value of the residuals to the sum of the absolute value of the individual terms in the inversion-layer budget equations. We tested several ratios of this general type and found the above ratio works well.

The value of ϕ is obtained with the jump values, the entrainment rate given by (E7) with the diagnosed z_{B+}, and all possible choices of level B below level $B+$. In Fig. E1c, the level of the minimum is reasonably fit as level B in the soundings shown in Fig. E1a. Further analysis suggested that the minimum tends to locate at the level B if the number of minima is one. If number of minima is more than one, the first minimum tends to

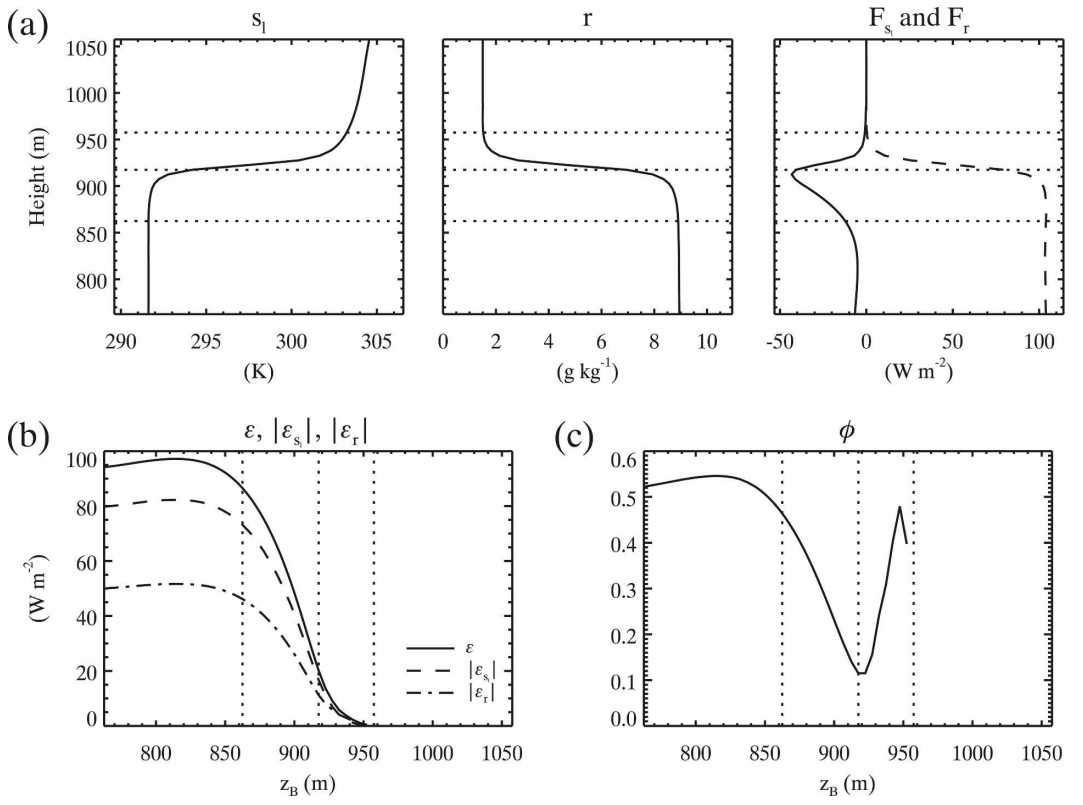

FIG. E1. (a) Vertical profiles of liquid water static energy, total mixing ratio, and their fluxes (solid line for s_l and dashed line for r). (b) Residuals with fixed z_{B+} and all possible choices of z_B. (c) Profile of ϕ at this time. All plots are produced with the data at hour 10 of DYCOMS-II simulation. Diagnosed levels z_{B+} and z_B and the level of 0.9 z_{B+} are shown with the dotted lines.

occur in the inversion layer, and the second minimum tends to occur at $z = z_B$. Thus, we choose level B as

> the level of the first minimum of ϕ, if number of minima is one or
> the level of the second minimum of ϕ, otherwise. (E10)

We apply this search method between z_{B+} and 0.9 z_{B+} to eliminate too-low-level B diagnosed with the second minimum.

The time series of the diagnosed z_B fluctuates more than that of the diagnosed z_{B+}. To obtain a smoother solution, we applied a 30-min running median filter and then a 30-min running mean to both diagnosed z_{B+} and z_B. After this smoothing process, jump values are computed with the interpolation value for each level, then the entrainment rate is obtained with (E7).

REFERENCES

Albrecht, B. A., 1991: Fractional cloudiness and cloud-top entrainment instability. *J. Atmos. Sci.,* **48,** 1519–1525.

——, R. S. Penc, and W. H. Schubert, 1985: An observational study of cloud-topped mixed layers. *J. Atmos. Sci.,* **42,** 800–822.

Bretherton, C. S., and M. C. Wyant, 1997: Moisture transport, lower-tropospheric stability, and decoupling of cloud-topped boundary layers. *J. Atmos. Sci.,* **54,** 148–167.

——, and Coauthors, 1999: An intercomparison of radiatively driven entrainment and turbulence in a smoke cloud, as simulated by different numerical models. *Quart. J. Roy. Meteor. Soc.,* **125,** 391–423.

Deardorff, J. W., 1980: Cloud top entrainment instability. *J. Atmos. Sci.,* **37,** 131–147.

Durran, D. R., 1991: The third-order Adams-Bashforth method: An attractive alternative to leapfrog time differencing. *Mon. Wea. Rev.,* **119,** 702–720.

Duynkerke, P. G., 1993: The stability of cloud top with regard to entrainment: Amendment of the theory of cloud-top entrainment instability. *J. Atmos. Sci.,* **50,** 495–502.

Gerber, H., G. Frick, S. P. Malinowski, J.-L. Brenguier, and F. Burnet, 2005: Holes and entrainment in stratocumulus. *J. Atmos. Sci.,* **62,** 443–459.

Hanson, H. P., 1984a: Stratocumulus instability reconsidered: A search for physical mechanisms. *Tellus,* **36A,** 355–368.

——, 1984b: On mixed-layer modeling of the stratocumulus-topped marine boundary layer. *J. Atmos. Sci.,* **41,** 1226–1234.

Khairoutdinov, M. F., and Y. L. Kogan, 1999: A large eddy simulation model with explicit microphysics: Validation against

aircraft observations of a stratocumulus-topped boundary layer. *J. Atmos. Sci.,* **56,** 2115–2131.

——, and ——, 2000: A new cloud physics parameterization in a large-eddy simulation model of marine stratocumulus. *Mon. Wea. Rev.,* **128,** 229–243.

——, and D. A. Randall, 2003: Cloud resolving modeling of the ARM summer 1997 IOP: Model formulation, results, uncertainties, and sensitivities. *J. Atmos. Sci.,* **60,** 607–625.

Khalsa, S. J. S., 1993: Direct sampling of entrainment events in a marine stratocumulus layer. *J. Atmos. Sci.,* **50,** 1734–1750.

Kiehl, J. T., J. J. Hack, G. B. Bonan, B. A. Boville, D. L. Williamson, and P. J. Rasch, 1998: The National Center for Atmospheric Research Community Climate Model: CCM3. *J. Climate,* **11,** 1131–1149.

Krueger, S. K., 1993: Linear eddy modeling of entrainment and mixing in stratus clouds. *J. Atmos. Sci.,* **50,** 3078–3090.

Kuo, H.-C., and W. H. Schubert, 1988: Stability of cloud-topped boundary layers. *Quart. J. Roy. Meteor. Soc.,* **114,** 887–916.

Lewellen, D. C., and W. S. Lewellen, 1998: Large-eddy boundary layer entrainment. *J. Atmos. Sci.,* **55,** 2645–2665.

Lilly, D. K., 1968: Models of cloud-topped mixed layers under a strong inversion. *Quart. J. Roy. Meteor. Soc.,* **94,** 292–309.

——, 2002: Entrainment into mixed layers. Part II: A new closure. *J. Atmos. Sci.,* **59,** 3353–3361.

Lock, A. P., and M. K. MacVean, 1999: The generation of turbulence and entrainment by buoyancy reversal. *Quart. J. Roy. Meteor. Soc.,* **125,** 1017–1038.

MacVean, M. K., 1993: A numerical investigation of the criterion for cloud-top entrainment instability. *J. Atmos. Sci.,* **50,** 2481–2495.

——, and P. J. Mason, 1990: Cloud-top entrainment instability through small-scale mixing and its parameterization in numerical models. *J. Atmos. Sci.,* **47,** 1012–1030.

Mahrt, L., and J. Paumier, 1982: Cloud-top entrainment instability observed in AMTEX. *J. Atmos. Sci.,* **39,** 622–634.

Moeng, C.-H., 2000: Entrainment rate, cloud fraction, and liquid water path of PBL stratocumulus clouds. *J. Atmos. Sci.,* **57,** 3627–3643.

——, and A. Arakawa, 1980: A numerical study of a marine subtropical stratus cloud layer and its stability. *J. Atmos. Sci.,* **37,** 2661–2676.

——, D. H. Lenschow, and D. A. Randall, 1995: Numerical investigations of the roles of radiative and evaporative feedbacks in stratocumulus entrainment and breakup. *J. Atmos. Sci.,* **52,** 2869–2883.

——, and Coauthors, 1996: Simulation of a stratocumulus-topped planetary boundary layer: Intercomparison among different numerical codes. *Bull. Amer. Meteor. Soc.,* **77,** 261–278.

——, B. Stevens, and P. P. Sullivan, 2005: Where is the interface of the stratocumulus-topped PBL? *J. Atmos. Sci.,* **62,** 2626–2631.

Monin, A. S., and A. M. Obukhov, 1954: Basic laws of turbulent mixing in the atmosphere near the ground. *Tr. Akad. Nauk SSSR Geophiz. Inst.,* **24,** 163–187.

Nicholls, S., and J. D. Turton, 1986: An observational study of the structure of stratiform cloud sheets: Part II. Entrainment. *Quart. J. Roy. Meteor. Soc.,* **112,** 461–480.

Randall, D. A., 1976: The interaction of the planetary boundary layer with large-scale circulations. Ph.D. dissertation, University of California, Los Angeles, 247 pp.

——, 1980: Conditional instability of the first kind upside-down. *J. Atmos. Sci.,* **37,** 125–130.

——, 1984: Stratocumulus cloud deepening through entrainment. *Tellus,* **36A,** 446–457.

Shao, Q., D. A. Randall, C.-H. Moeng, and R. E. Dickinson, 1997: A method to determine the amounts of cloud-top radiative and evaporative cooling in a stratocumulus-topped boundary layer. *Quart. J. Roy. Meteor. Soc.,* **123,** 2187–2213.

Shy, S. S., and R. E. Breidenthal, 1990: Laboratory experiments on the cloud-top entrainment instability. *J. Fluid Mech.,* **214,** 1–15.

Siebesma, A. P., and Coauthors, 2003: A large eddy simulation intercomparison study of shallow cumulus convection. *J. Atmos. Sci.,* **60,** 1201–1219.

Siems, S. T., and C. S. Bretherton, 1992: A numerical investigation of cloud-top entrainment instability and related experiments. *Quart. J. Roy. Meteor. Soc.,* **118,** 787–818.

——, ——, M. B. Baker, S. S. Shy, and R. E. Breidenthal, 1990: Buoyancy reversal and cloud-top entrainment instability. *Quart. J. Roy. Meteor. Soc.,* **116,** 705–739.

Squires, P., 1958: Penetrative downdraughts in cumuli. *Tellus,* **10,** 381–389.

Stevens, B., and Coauthors, 2003: Dynamics and Chemistry of Marine Stratocumulus—DYCOMS-II. *Bull. Amer. Meteor. Soc.,* **84,** 579–593.

——, and Coauthors, 2005: Evaluation of large-eddy simulations via observations of nocturnal marine stratocumulus. *Mon. Wea. Rev.,* **133,** 1443–1462.

Tag, P. M., and S. W. Payne, 1987: An examination of the breakup of marine stratus: A three-dimensional numerical investigation. *J. Atmos. Sci.,* **44,** 208–223.

Turton, J. D., and S. Nicholls, 1987: A study of the diurnal variation of stratocumulus using a multiple mixed layer model. *Quart. J. Roy. Meteor. Soc.,* **113,** 969–1009.

Wang, Q., and B. A. Albrecht, 1994: Observations of cloud-top entrainment in marine stratocumulus clouds. *J. Atmos. Sci.,* **51,** 1530–1547.

Weaver, C. J., and R. Pearson, 1990: Entrainment instability and vertical motion as causes of stratocumulus breakup. *Quart. J. Roy. Meteor. Soc.,* **116,** 1359–1388.